TIME-DEPENDENT DIELECTRIC RESPONSE OF POLYMER NANOPARTICULATE COMPOSITES CONTAINING RAPIDLY OSCILLATING SOURCE TERMS

BY

JINLONG GUO

THESIS

Submitted in partial fulfillment of the requirements
for the degree of Master of Science in Civil Engineering
with a concentration in Computational Science and Engineering
in the Graduate College of the
University of Illinois at Urbana-Champaign, 2019

Urbana, Illinois

Adviser:

Associate Professor Oscar Lopez-Pamies

ABSTRACT

This thesis presents the derivation of the homogenized equations for the macroscopic response of time-dependent dielectric composites that contain space charges varying spatially at the length scale of the microstructure and that are subjected to alternating electric fields. The focus is on dielectrics with periodic microstructures and two fairly general classes of space charges: passive (or fixed) and active (or locally mobile). With help of a standard change of variables, in spite of the presence of space charges, the derivation amounts to transcribing a previous two-scale-expansion result introduced in Lefèvre and Lopez-Pamies (2017a) for perfect dielectrics to the realm of complex frequency-dependent dielectrics. With the objectives of illustrating their use and of showcasing their ability to describe and explain the macroscopic response of emerging materials featuring extreme dielectric behaviors, the derived homogenization results are deployed to examine dielectric spectroscopy experiments on various polymer nanoparticulate composites. It is found that so long as space charges are accounted for, the proposed theoretical results are able to describe and explain all the experimental results. By the same token, more generally, these representative comparisons with experiments point to the manipulation of space charges at small length scales as a promising strategy for the design of materials with exceptional macroscopic properties.

To my parents, for their love and support.

ACKNOWLEDGMENTS

Foremost, I would like to express my deepest appreciation to my thesis adviser Professor Oscar Lopez-Pamies, for his patience, enthusiasm, and immense knowledge. He showed and taught me how to do a good research in the realm of Mechanics as the most elegant and concise way as I have known so far. I could not have imagined having a better adviser and mentor for my Master study.

I would also like to thank my colleagues: Kamalendu Ghosh, for his tremendous contribution to this work and inspiring discussions during the year; Bhavesh Shrimali, for his invaluable help to my coursework and graduate study; Aditya Kumar, for providing useful suggestions during my graduate life.

Last but not the least, I would like to express my profound gratitute to my parents and family for providing me with unending support and continuous encouragement throughout these years.

TABLE OF CONTENTS

CHAPTER 1

INTRODUCTION

Dielectric elastomers are multifunctional materials, which have been of recent increasing interest in a variety of applications, such as actuators, energy harvesters, and sensors; see, e.g., the books by Bar-Cohen (2004) and Carpi and Smela (2009). Their flexibility, light weight, and biocompatibility among other attractive features, have motivated their possible use. Unfortunately, it requires high electric fields (in the order of $100\text{V}/\mu\text{m}$) to obtain considerable electrostrictive deformations in this kind of materials; see e.g., Brochu and Pei (2013). To address this shortcoming, over the last decade, a number of experiments have demonstrated that the addition of nanoparticles to a dielectric elastomer may generate a drastic enhancement of their dielectric response, which entails that electrostrictive deformations would happen under weaker electric fields. In some other research works, however, a reduction of the macroscopic permittivity was observed as well.

To gain insight into the above-outlined experiments, in this thesis, we concern ourselves with the determination of the homogenized equations for time-dependent dielectric composites, containing space charges that vary spatially at the length scale of the microstructure, under alternating electric fields. The work is, in a sense, a generalization of that of Lefèvre and Lopez-Pamies (2017a), who considered the analogous problem in the time-independent setting of perfect dielectrics. Like in that work, the focus is on dielectrics with periodic microstructures and on two fairly general classes of space charges: *passive* and *active*.

Passive charges refer to *fixed* space charges that are present within the dielectric from its fabrication process. Arguably, the most prominent type of materials that can be regarded as dielectrics containing passive space charges are the so-called electrets; see, e.g., Kestelman et al. (2000) and Bauer et al. (2004). On the other hand, active space charges refer to *locally mobile* space charges that are not present from the outset but that, instead, "appear" as

a result of externally applied electric fields or currents. Polymers filled with nanoparticles, featuring in one way or another extreme dielectric behaviors, are thought to be examples of materials that can be viewed as dielectrics containing active space charges; see, e.g., Lewis (2004) and Lopez-Pamies et al. (2014).

The thesis is organized as follows. We begin in Chapter 2 by formulating the local initial-boundary-value problem to be homogenized. Through a standard change of variables, in spite of the presence of source terms (i.e., space charges), this time-dependent problem is recast as a *time-independent boundary-value problem*, given by Eqs. (2.9), for a complex scalar field $\widetilde{\varphi}^{\delta}(\mathbf{X},\omega)$ that fully characterizes the harmonic steady-state electric potential in the dielectric composite under consideration. In Chapter 3, we then work out the homogenization limit of the governing equations (2.9) for $\widetilde{\varphi}^{\delta}(\mathbf{X},\omega)$ when the size of the microstructure $\delta \to 0$ for the case of passive charges. This is accomplished by exploiting the similar mathematical structure of the governing equations here with those studied by Lefèvre and Lopez-Pamies (2017a) for time-independent dielectrics. In turn, we work out in Chapter 4 the homogenization limit for the case of active charges, in particular, when the space charges are active in the sense that they are proportional to the resulting macroscopic electric field. In Chapter 5, we spell out the specialization of the effective complex permittivity $\widetilde{\boldsymbol{\varepsilon}}^{\star}(\omega)$ that emerges in the homogenized equations for the case of active charges to a broad class of isotropic particulate composite materials. In Chapter 6, we deploy the results for $\widetilde{\boldsymbol{\varepsilon}}^{\star}(\omega)$ put forth in Chapter 5 to compare with and examine dielectric spectroscopy experiments on various polymer nanoparticulate composites. Finally, in Chapter 7 we discuss the main conclusions from the ensuing comparisons on theoretical and practical implications.

CHAPTER 2

THE PROBLEM

Consider a dielectric composite material with periodic microstructure of period δ that occupies a bounded domain $\Omega \subset \mathbb{R}^N$ $(N = 1, 2, 3)$, with smooth boundary $\partial\Omega$ and closure $\overline{\Omega} = \Omega \cup \partial\Omega$. In this thesis, we restrict attention to initial-boundary-value problems when the given dielectric of interest, schematically depicted in Fig. 2.1, does *not* deform.

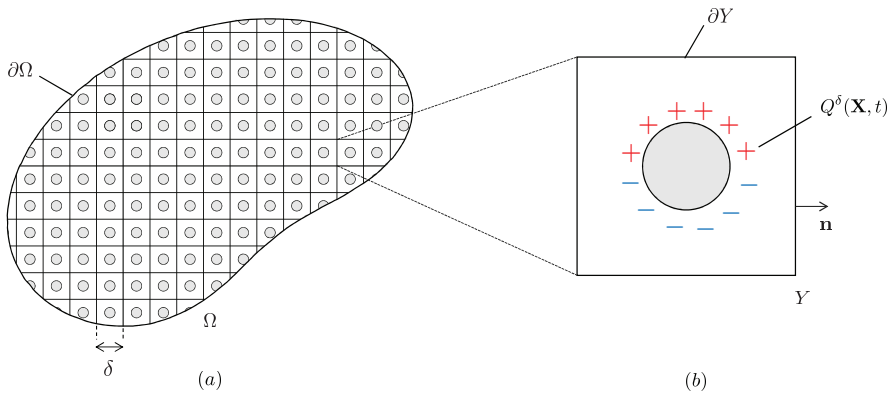

Figure 2.1: (a) Schematic of a dielectric composite material containing a distribution of space charges that vary spatially at the length scale of the microstructure δ. (b) Schematic of the unit cell $Y = (0, 1)^N$ that defines the periodic microstructure (of period δ) of the dielectric with the explicit illustration of the distribution of space charges characterized by the time-dependent space-charge density $Q^\delta(\mathbf{X}, t)$.

Constitutive behavior The constitutive relation between the electric displacement $\mathbf{D}^\delta(\mathbf{X}, t)$ and the electric field $\mathbf{E}^\delta(\mathbf{X}, t)$ at any given material point $\mathbf{X} \in \Omega$ and time $t \in [0, T]$ is taken to be given by the linear causal relation[1]

$$D_k^\delta(\mathbf{X}, t) = \int_{-\infty}^{t} \varepsilon_{kl}^\delta(\mathbf{X}, t - \tau) \frac{\partial E_l^\delta}{\partial \tau}(\mathbf{X}, \tau) \mathrm{d}\tau. \tag{2.1}$$

[1]Throughout this thesis, unless otherwise stated, we employ the Einstein summation convention.

Precisely, with help of the notation $Y = (0,1)^N$, the time-dependent permittivity tensor $\boldsymbol{\varepsilon}^\delta(\mathbf{X},t)$ is taken to be of the form

$$\varepsilon_{kl}^\delta(\mathbf{X},t) \in \mathbb{R} \qquad \text{and} \qquad \varepsilon_{kl}^\delta(\mathbf{X},t) = \varepsilon_{kl}(\delta^{-1}\mathbf{X},t) \quad \text{with} \quad \varepsilon_{kl}(\mathbf{y},\omega)\ Y-\text{periodic.}$$

Basic physical considerations[2] dictate that

$$\varepsilon_{kl}^\delta(\mathbf{X},t) = \varepsilon_{lk}^\delta(\mathbf{X},t) \qquad \text{and} \qquad \varepsilon_{kl}^\delta(\mathbf{X},t)\xi_k\xi_l \geq \varepsilon_0\xi_m\xi_m \ \ \forall\, \boldsymbol{\xi} \neq \mathbf{0},$$

where $\varepsilon_0 \approx 8.85 \times 10^{-12}$ F/m stands for the permittivity of vacuum.

Boundary conditions For later direct comparison with dielectric spectroscopy experiments (see, e.g., the book edited by Friedrich and Schönhals (2003)), we consider further that the dielectric is subjected to a prescribed electric potential or voltage, over the entirety of its boundary, which is independent of the size of the microstructure and, more specifically, is of the time harmonic form

$$\phi(\mathbf{X},t) = \widetilde{\phi}(\mathbf{X},\omega)e^{i\omega t}, \qquad (\mathbf{X},t) \in \partial\Omega \times [0,T], \tag{2.2}$$

where ω is the angular frequency, $i = \sqrt{-1}$, and the function $\widetilde{\phi}(\mathbf{X},\omega) \in \mathbb{C}$.

Source term Moreover, following Lefèvre and Lopez-Pamies (2017a), we consider that the dielectric contains a distribution of space charges that vary spatially at the length scale of the microstructure and its density (per unit volume) is of the following *divergence form* in space and *harmonic form* in time:

$$Q^\delta(\mathbf{X},t) = \widetilde{Q}^\delta(\mathbf{X},\omega)e^{i\omega t}, \qquad (\mathbf{X},t) \in \Omega \times [0,T] \tag{2.3}$$

[2]Here and subsequently, we will refrain from digressing into mathematical considerations, such as stating the appropriate functional spaces for the various variables involved.

with

$$\begin{aligned}\widetilde{Q}^{\delta}(\mathbf{X},\omega) =& -\delta\frac{\partial}{\partial X_l}\left[f_k(\mathbf{X},\omega)\frac{\partial}{\partial X_l}\left[\psi_k(\delta^{-1}\mathbf{X},\omega)\right]\right]\\ =&\delta^{-1}f_k(\mathbf{X},\omega)g_k(\delta^{-1}\mathbf{X},\omega)-\frac{\partial f_k}{\partial X_l}(\mathbf{X},\omega)\tau_{kl}(\delta^{-1}\mathbf{X},\omega).\end{aligned}\tag{2.4}$$

Here, $\mathbf{f}(\mathbf{X},\omega)\in\mathbb{C}^N$ is any arbitrary function of choice, $\mathbf{g}(\mathbf{y},\omega)\in\mathbb{C}^N$ is any $Y-$periodic function of choice such that

$$\int_Y \mathbf{g}(\mathbf{y},\omega)\,\mathrm{d}\mathbf{y}=\mathbf{0},\tag{2.5}$$

while $\tau_{kl}(\mathbf{y},\omega)=\partial\psi_k(\mathbf{y},\omega)/\partial y_l$ with $\boldsymbol{\psi}(\mathbf{y},\omega)$ defined in terms of $\mathbf{g}(\mathbf{y},\omega)$ as the unique solution of the linear elliptic boundary-value problem

$$\begin{cases}-\dfrac{\partial^2\psi_k}{\partial y_l\partial y_l}(\mathbf{y},\omega)=g_k(\mathbf{y},\omega), \quad \mathbf{y}\in Y\\ -\dfrac{\partial\psi_k}{\partial y_l}(\mathbf{y},\omega)n_l=0, \quad \mathbf{y}\in\partial Y\\ \int_Y\psi_k(\mathbf{y},\omega)\mathrm{d}\mathbf{y}=0\end{cases},\tag{2.6}$$

where $\mathbf{n}$ in $(2.6)_2$ stands for the outward unit normal to the boundary ∂Y of the unit cell Y; see Fig. 2.1(b). Note that the form (2.4) comprises two *constitutive inputs*: the functions $\mathbf{f}(\mathbf{X},\omega)$ and $\mathbf{g}(\delta^{-1}\mathbf{X},\omega)$. Roughly speaking, the latter dictates the local distribution of charges at the microscopic length scale δ of each unit cell. The former, on the other hand, dictates the possibly non-uniform distribution of charges at the macroscopic length scale of Ω. As it will become more apparent further below in the comparisons with experiments, the choice of space-charge density (2.4) has the merit to be functionally rich enough to be able to describe a range of experimental observations.

The governing equations In the setting of electro-quasistatics, when the time derivative of the magnetic induction $\partial\mathbf{B}^{\delta}/\partial t$ is negligibly small, direct use of the constitutive relation (2.1), boundary conditions (2.2), and source term (2.3) in the relevant equations of Maxwell

(see, e.g., Chapter X in the monograph by Owen (2003))

$$\operatorname{Div}\mathbf{D}^{\delta}(\mathbf{X},t)=Q^{\delta}(\mathbf{X},t)\qquad\text{and}\qquad\operatorname{Curl}\mathbf{E}^{\delta}(\mathbf{X},t)=0$$

can be readily shown to reduce to the initial-boundary-value problem

$$\begin{cases}\dfrac{\partial}{\partial X_k}\left[-\displaystyle\int_{-\infty}^{t}\varepsilon_{kl}(\delta^{-1}\mathbf{X},t-\tau)\frac{\partial^2\varphi^{\delta}}{\partial\tau\partial X_l}(\mathbf{X},\tau)\mathrm{d}\tau\right]=\widetilde{Q}^{\delta}(\mathbf{X},\omega)e^{i\omega t},\quad(\mathbf{X},t)\in\Omega\times[0,T]\\ \varphi^{\delta}(\mathbf{X},t)=\widetilde{\phi}(\mathbf{X},\omega)e^{i\omega t},\quad(\mathbf{X},t)\in\partial\Omega\times[0,T]\end{cases}\tag{2.7}$$

for the electric potential $\varphi^{\delta}(\mathbf{X},t)$, defined here so that $E_l^{\delta}(\mathbf{X},t)=-\partial\varphi^{\delta}(\mathbf{X},t)/\partial X_l$. Note that the restriction of the governing PDE $(2.7)_1$ to the domain Ω occupied by the dielectric (as opposed to the entire space $\mathbb{R}^N$ where Maxwell's equations ought to be solved) is sufficient in the present context thanks to the prescription of the Dirichlet boundary condition $(2.7)_2$. Of course, we are only interested in the real part of (2.7), but, for algebraic expediency and relatively more elegance, dealing throughout with complex-value quantities is preferable.

The focus of this thesis is on the harmonic steady-state solution of the initial-boundary-value problem (2.7) at sufficiently large times $t>0$, once the transient terms associated with the applied boundary data and source term have effectively vanished. We thus look for solutions to (2.7) of the form

$$\varphi^{\delta}(\mathbf{X},t)=\widetilde{\varphi}^{\delta}(\mathbf{X},\omega)e^{i\omega t}.\tag{2.8}$$

Substituting this last expression in the equations (2.7) and subsequently carrying out standard algebraic manipulations (see, e.g., Gross (1953); Chapter VIII in Böttcher and Bordewijk (1978)) renders the following boundary-value problem:

$$\begin{cases}\dfrac{\partial}{\partial X_k}\left[-\widetilde{\varepsilon}_{kl}(\delta^{-1}\mathbf{X},\omega)\dfrac{\partial\widetilde{\varphi}^{\delta}}{\partial X_l}(\mathbf{X},\omega)\right]=\widetilde{Q}^{\delta}(\mathbf{X},\omega),\quad\mathbf{X}\in\Omega\\ \widetilde{\varphi}^{\delta}(\mathbf{X},\omega)=\widetilde{\phi}(\mathbf{X},\omega),\quad\mathbf{X}\in\partial\Omega\end{cases}\tag{2.9}$$

for the function $\widetilde{\varphi}^{\delta}(\mathbf{X},\omega)$ characterizing the space-varying part of the harmonic electric

potential (2.8) in the steady state, where

$$\widetilde{\varepsilon}_{kl}(\delta^{-1}\mathbf{X},\omega) = i\omega \int_0^\infty \varepsilon_{kl}(\delta^{-1}\mathbf{X},z)e^{-i\omega z}\mathrm{d}z \tag{2.10}$$

happens to correspond to a one-sided Fourier transform of the time-dependent permittivity tensor $\boldsymbol{\varepsilon}(\delta^{-1}\mathbf{X},t)$ and where it is recalled that the function $\widetilde{Q}^\delta(\mathbf{X},\omega)$ is given by expression (2.4) in terms of δ and the two constitutive inputs $\mathbf{f}(\mathbf{X},\omega)$ and $\mathbf{g}(\delta^{-1}\mathbf{X},\omega)$.

The governing equations (2.9) for the complex field $\widetilde{\varphi}^\delta(\mathbf{X},\omega)$ feature the same mathematical structure as the governing equations for the real electric potential in a *time-independent* dielectric composite material that contains *time-independent* space charges, with density of the form (2.4), varying spatially at the length scale of the microstructure and that is subjected to a prescribed electric potential on its boundary, c.f., Eq. (8) in Lefèvre and Lopez-Pamies (2017a); the only two differences are that the constitutive properties, boundary conditions, and source term in (2.9) are of complex value and, in addition, are parameterized by ω, which, again, stands for the angular frequency chosen for the applied loading. Accordingly, much like in the classical setting of dielectrics containing *no* space charges (see, e.g., the classical works of Wagner (1914); Sillars (1936); Hashin (1983)), the same techniques of solution used for the time-independent and conservative problem apply *mutatis mutandis* to the *time-dependent* and dissipative problem of interest here.

In the next two Chapters, we make use of the results put forth in Lefèvre and Lopez-Pamies (2017a) to determine the homogenization limit of the governing equations (2.9) when the period of the microstructure $\delta \to 0$. Chapter 3 deals with the case of *passive* space charges, while Chapter 4 deals with the case of *active* space charges when, in particular, the function $\mathbf{f}(\mathbf{X},\omega)$ in (2.4) is taken to be proportional to the resulting macroscopic field for the electric potential.

CHAPTER 3

THE HOMOGENIZED EQUATIONS FOR THE CASE OF PASSIVE CHARGES

By suitably transcribing the results put forth in Section 2 of Lefèvre and Lopez-Pamies (2017a), it is a simple matter to deduce that in the limit as the period of the microstructure $\delta \to 0$ the solution $\widetilde{\varphi}^\delta(\mathbf{X},\omega)$ of the boundary-value problem (2.9) is given asymptotically by

$$\begin{aligned}\widetilde{\varphi}^\delta(\mathbf{X},\omega) = \widetilde{\varphi}(\mathbf{X},\omega) - \delta\left(\chi_p\left(\delta^{-1}\mathbf{X},\omega\right)\frac{\partial\widetilde{\varphi}}{\partial X_p}(\mathbf{X},\omega) + \Theta_p\left(\delta^{-1}\mathbf{X},\omega\right) f_p(\mathbf{X},\omega) + \widetilde{\varphi}^\delta_{BL}(\mathbf{X},\omega)\right) \\ + O(\delta^2),\end{aligned} \tag{3.1}$$

where $\chi_p(\mathbf{y},\omega)$ and $\Theta_p(\mathbf{y},\omega)$ are the Y-periodic functions defined implicitly as the unique solutions of the linear elliptic PDEs

$$\begin{cases} \dfrac{\partial}{\partial y_k}\left[\widetilde{\varepsilon}_{kl}\left(\mathbf{y},\omega\right)\dfrac{\partial\chi_p}{\partial y_l}(\mathbf{y},\omega)\right] = \dfrac{\partial\widetilde{\varepsilon}_{kp}}{\partial y_k}\left(\mathbf{y},\omega\right), \quad \mathbf{y}\in Y \\ \int_Y \chi_p(\mathbf{y},\omega)\mathrm{d}\mathbf{y} = 0 \end{cases} \tag{3.2}$$

and

$$\begin{cases} \dfrac{\partial}{\partial y_k}\left[\widetilde{\varepsilon}_{kl}\left(\mathbf{y},\omega\right)\dfrac{\partial\Theta_p}{\partial y_l}(\mathbf{y},\omega)\right] = g_p(\mathbf{y},\omega), \quad \mathbf{y}\in Y \\ \int_Y \Theta_p(\mathbf{y},\omega)\mathrm{d}\mathbf{y} = 0 \end{cases}, \tag{3.3}$$

$\widetilde{\varphi}^\delta_{BL}(\mathbf{X},\omega)$ is the function needed to conform with possible boundary layer effects, and where, more importantly, the leading order term $\widetilde{\varphi}(\mathbf{X},\omega)$ is defined implicitly by the following

boundary-value problem:

$$\begin{cases} \dfrac{\partial}{\partial X_k}\left[-\widetilde{\varepsilon}^*_{kl}(\omega)\dfrac{\partial\widetilde{\varphi}}{\partial X_l}(\mathbf{X},\omega)\right] = \widetilde{Q}^*(\mathbf{X},\omega), \quad \mathbf{X}\in\Omega \\ \widetilde{\varphi}(\mathbf{X},\omega) = \widetilde{\phi}(\mathbf{X},\omega), \quad \mathbf{X}\in\partial\Omega \end{cases} . \tag{3.4}$$

Here,

$$\widetilde{\varepsilon}^*_{kl}(\omega) = \int_Y \widetilde{\varepsilon}_{kp}(\mathbf{y},\omega)\left(\delta_{lp} - \frac{\partial\chi_l}{\partial y_p}(\mathbf{y},\omega)\right)\mathrm{d}\mathbf{y} \qquad \text{and} \qquad \widetilde{Q}^*(\mathbf{X},\omega) = -\frac{\partial}{\partial X_k}\left[\alpha^*_{kl}(\omega) f_l(\mathbf{X},\omega)\right] \tag{3.5}$$

with

$$\begin{aligned} \alpha^*_{kl}(\omega) &= \int_Y \left(\varepsilon_{kp}(\mathbf{y},\omega)\frac{\partial\Theta_l}{\partial y_p}(\mathbf{y},\omega) + y_k g_l(\mathbf{y},\omega)\right)\mathrm{d}\mathbf{y} \\ &= \int_Y \left(y_k - \chi_k(\mathbf{y},\omega)\right) g_l(\mathbf{y},\omega)\mathrm{d}\mathbf{y}. \end{aligned} \tag{3.6}$$

Equations (3.4) are nothing more than the homogenized equations for the *macroscopic* field $\widetilde{\varphi}(\mathbf{X},\omega)$ characterizing the sought after steady-state harmonic solution (2.8), precisely,

$$\varphi^\delta(\mathbf{X},t) = \widetilde{\varphi}(\mathbf{X},\omega)e^{i\omega t} + O(\delta),$$

of the initial-boundary-value problem (2.7) in the limit of separation of length scales when the characteristic size of the microstructure δ is much smaller than the macroscopic size of the dielectric composite material Ω.

The following remarks are in order:

i. Physical interpretation of the homogenized equations (3.4). Equations (3.4) correspond to the governing equations for the complex electric potential $\widetilde{\varphi}(\mathbf{X},\omega)$ within a *homogeneous* dielectric medium, with effective complex permittivity tensor $\widetilde{\boldsymbol{\varepsilon}}^*(\omega)$, which contains a *non-homogeneous* distribution of space charges characterized by the effective complex space-charge density $\widetilde{Q}^*(\mathbf{X},\omega)$ and is subjected to Dirichlet boundary conditions.

Besides identifying the field $\widetilde{\varphi}(\mathbf{X},\omega)$ as the relevant *macro-variable* for the complex electric potential, glancing at (3.4) also suffices to recognize that the *macro-variables* for the corresponding complex electric field and the electric displacement are given by

$$\widetilde{E}_k(\mathbf{X},\omega) \doteq -\frac{\partial\widetilde{\varphi}}{\partial X_k}(\mathbf{X},\omega) \qquad \text{and} \qquad \widetilde{D}_k(\mathbf{X},\omega) \doteq -\widetilde{\varepsilon}^*_{kl}(\omega)\frac{\partial\widetilde{\varphi}}{\partial X_l}(\mathbf{X},\omega). \tag{3.7}$$

Here, it is insightful to notice that in terms of the *local* electric field

$$\widetilde{E}^\delta_k(\mathbf{X},\omega) = -\frac{\partial\widetilde{\varphi}^\delta}{\partial X_k}(\mathbf{X},\omega) = \widetilde{E}^{(0)}_k\left(\mathbf{X},\delta^{-1}\mathbf{X},\omega\right) + O\left(\delta\right), \tag{3.8}$$

with $\widetilde{E}^{(0)}_k\left(\mathbf{X},\mathbf{y},\omega\right) = -\partial\widetilde{\varphi}(\mathbf{X},\omega)/\partial X_k + \left(\partial\widetilde{\varphi}(\mathbf{X},\omega)/\partial X_p\right)\left(\partial\widetilde{\chi}_p(\mathbf{y},\omega)/\partial y_k\right)$
$+ f_p(\mathbf{X},\omega)\partial\widetilde{\Theta}_p(\mathbf{y},\omega)/\partial y_k$, and the *local* electric displacement

$$\widetilde{D}^\delta_k(\mathbf{X},\omega) = \widetilde{\varepsilon}_{kl}\left(\delta^{-1}\mathbf{X},\omega\right)\widetilde{E}^\delta_l\left(\mathbf{X},\omega\right) = \widetilde{D}^{(0)}_k\left(\mathbf{X},\delta^{-1}\mathbf{X},\omega\right) + O\left(\delta\right), \tag{3.9}$$

the macro-variables (3.7) read as

$$\widetilde{E}_k(\mathbf{X},\omega) = \int_Y \widetilde{E}^{(0)}_k\left(\mathbf{X},\mathbf{y},\omega\right)\mathrm{d}\mathbf{y} \tag{3.10}$$

and

$$\widetilde{D}_k(\mathbf{X},\omega) = \int_Y \widetilde{D}^{(0)}_k\left(\mathbf{X},\mathbf{y},\omega\right)\mathrm{d}\mathbf{y} + \left(\int_Y \chi_k(\mathbf{y},\omega)g_l(\mathbf{y},\omega)\mathrm{d}\mathbf{y}\right) f_l(\mathbf{X},\omega). \tag{3.11}$$

Expression (3.10) indicates that the macro-variable $(3.7)_1$ coincides with the macro-variable found in the absence of space charges, namely, it corresponds to the average over the unit cell Y of the leading-order term of the local electric field, here, $\widetilde{E}^\delta_k(\mathbf{X},\omega)$; see, e.g., Chapter 2 in Bensoussan et al. (2011). From (3.11), we see that the same is *not* true about the macro-variable $(3.7)_2$ for the electric displacement, which in addition to the average over the unit cell Y of the leading-order term of the local electric displacement features a contribution due to the presence of space charges. This additional contribution is nothing but the expected manifestation of the fact that

the local electric displacement is no longer divergence free in the presence of space charges.

ii. The effective complex permittivity tensor $\widetilde{\boldsymbol{\varepsilon}}^*(\omega)$. The effective complex permittivity tensor $(3.5)_1$ in the homogenized equations (3.4) is the standard effective permittivity that emerges in dielectric composite materials containing *no* space charges; see, e.g.,Sanchez-Hubert and Sanchez-Palencia (1978), Chapter 6 in Sanchez-Palencia (1980), and Section 6.4 in Hashin (1983). Accordingly, the result $(3.5)_1$ is independent of the domain Ω occupied by the dielectric, the boundary conditions on $\partial\Omega$, the presence of space charges, and it satisfies the standard properties

$$\widetilde{\varepsilon}^*_{kl} = \widetilde{\varepsilon}^*_{lk}(\omega), \qquad \mathrm{Re}\,\{\widetilde{\varepsilon}^*_{kl}(\omega)\}\,\xi_k\xi_l \geq \varepsilon_0\xi_m\xi_m \;\; \forall\,\boldsymbol{\xi} \neq \mathbf{0}$$

of the complex permittivity of a homogeneous dielectric medium.

From a practical point of view, we remark that the evaluation of the formula $(3.5)_1$ for $\widetilde{\boldsymbol{\varepsilon}}^*(\omega)$ requires knowledge of the Y-periodic function $\chi_k(\mathbf{y},\omega)$ defined by the boundary-value problem (3.2). While this problem does not admit an analytical solution in general, it can be readily solved numerically by a variety of methods, for instance, the finite element method.

iii. The effective complex space-charge density $\widetilde{Q}^*(\mathbf{X},\omega)$. The effective complex space-charge density $(3.5)_2$ with (3.6) in the homogenized equations (3.4) is independent of the domain Ω occupied by the dielectric and the boundary conditions on $\partial\Omega$, but depends on both of the constitutive functions $\mathbf{f}(\mathbf{X},\omega)$ and $\mathbf{g}(\delta^{-1}\mathbf{X},\omega)$ defining their local density (2.4). It is also worth noticing that the total content of macroscopic space charges implied by the effective complex space-charge density $(3.5)_2$ with (3.6),

$$\int_\Omega \widetilde{Q}^*(\mathbf{X},\omega)\mathrm{d}\mathbf{X} = -\int_\Omega \alpha^*_{kl}(\omega)\frac{\partial f_l}{\partial X_k}(\mathbf{X},\omega)\mathrm{d}\mathbf{X},$$

need *not* be zero. Indeed, only certain choices of the constitutive function $\mathbf{f}(\mathbf{X},\omega)$ render macroscopic charge neutrality.

According to the first equality in (3.6), evaluation of the formula $(3.5)_2$ for $\widetilde{Q}^*(\mathbf{X},\omega)$ requires knowledge of the Y-periodic function $\Theta_k(\mathbf{y},\omega)$ defined by the boundary-value problem (3.3). Remarkably, in view of the second equality in (3.6), which is a direct consequence of the divergence theorem and the Y–periodicity of the PDEs (3.2)–(3.3), the effective complex space-charge density $\widetilde{Q}^*(\mathbf{X},\omega)$ can also be obtained solely from knowledge of $\chi_k(\mathbf{y},\omega)$ without having to compute $\Theta_k(\mathbf{y},\omega)$.

iv. An alternative physical interpretation of the homogenized equations (3.4). In view of the divergence form of the effective complex effective-charge density $(3.5)_2$, the homogenized equations (3.4) can be rewritten in the alternative form

$$\begin{cases} \dfrac{\partial}{\partial X_k}\left[-\widetilde{\varepsilon}^*_{kl}(\omega)\dfrac{\partial\widetilde{\varphi}}{\partial X_l}(\mathbf{X},\omega)+\alpha^*_{kl}(\omega)f_l(\mathbf{X},\omega)\right]=0, \quad \mathbf{X}\in\Omega \\ \widetilde{\varphi}(\mathbf{X},\omega)=\widetilde{\phi}(\mathbf{X},\omega), \quad \mathbf{X}\in\partial\Omega \end{cases} . \tag{3.12}$$

The equivalent set of equations (3.12) correspond to the governing equations for the complex electric potential $\widetilde{\varphi}(\mathbf{X},\omega)$ within a *homogeneous* dielectric medium, with effective complex permittivity tensor $\widetilde{\boldsymbol{\varepsilon}}^*(\omega)$, that contains *no* space charges but that features instead a *non-homogeneous* effective complex pre-polarization characterized by the quantity $\alpha^*_{kl}(\omega)f_l(\mathbf{X},\omega)$, and that is subjected to Dirichlet boundary conditions.

In the form (3.12), much like in the form (3.4), the macro-variable for the complex electric field is still given by (3.10). However, the macro-variable for the complex electric displacement is now given by

$$\widetilde{D}_k(\mathbf{X},\omega) \doteq -\widetilde{\varepsilon}^*_{kl}(\omega)\frac{\partial\widetilde{\varphi}}{\partial X_l}(\mathbf{X},\omega)+\alpha^*_{kl}(\omega)f_l(\mathbf{X},\omega),$$

which in terms of the local electric displacement (3.9) reads as

$$\begin{aligned}\widetilde{D}_k(\mathbf{X},\omega) &= \int_Y \widetilde{D}^{(0)}_k(\mathbf{X},\mathbf{y},\omega)\,\mathrm{d}\mathbf{y}+\left(\int_Y y_k g_l(\mathbf{y},\omega)\mathrm{d}\mathbf{y}\right)f_l(\mathbf{X},\omega)\\ &= \int_{\partial Y} y_k\widetilde{D}^{(0)}_l(\mathbf{X},\mathbf{y},\omega)\,n_l\mathrm{d}\mathbf{y}.\end{aligned}$$

CHAPTER 4

THE HOMOGENIZED EQUATIONS FOR A CLASS OF ACTIVE CHARGES

The homogenized equations (3.4), or equivalently (3.12), are valid for arbitrary choices of the functions $\mathbf{f}(\mathbf{X},\omega)$ and $\mathbf{g}(\delta^{-1}\mathbf{X},\omega)$ characterizing the local space-charge density (2.4). In particular, these functions may be selected not to be fixed or *passive*, but to be *active* instead by designating them to depend in part or in full on the local complex electric potential $\widetilde{\varphi}^{\delta}(\mathbf{X},\omega)$. In this Chapter, following Lopez-Pamies et al. (2014) and Lefèvre and Lopez-Pamies (2017a), we consider a class of active charges wherein the function $\mathbf{g}(\delta^{-1}\mathbf{X},\omega)$ is taken to be arbitrary but fixed while the function $\mathbf{f}(\mathbf{X},\omega)$ is set to be proportional to the macroscopic complex electric field, precisely,

$$f_k(\mathbf{X},\omega) = -\frac{\partial\widetilde{\varphi}}{\partial X_k}(\mathbf{X},\omega). \tag{4.1}$$

From a physical point of view, the form (4.1) entails that at a macroscopic material point $\mathbf{X}$ the space charges, roughly speaking, scale in magnitude and align in direction with the complex electric field at that point. At present, there is little direct experimental knowledge about the constitutive behavior of active space charges in dielectrics. For instance, for the prominent case of polymers filled with (semi)conducting or dielectric nanoparticles, locally mobile space charges are expected to be present in the regions of the polymer immediately surrounding the nanoparticles (see, e.g., Lewis (2004); Roy et al. (2005); Nelson (2010); Lefèvre and Lopez-Pamies (2017c)), but direct measurements of the precise content and local mobility of these have proved thus far difficult. As elaborated further below in comparisons with various sets of experimental results (Huang et al. (2005); Thakur et al. (2017); Zhang et al. (2017);Nelson and Fothergill (2004); Fothergill et al. (2004)), the prescription (4.1) can be thought of perhaps as the simplest physically plausible prototype that is consistent

with the available macroscopic experimental measurements.

Now, granted the choice (4.1) for the function $\mathbf{f}(\mathbf{X},\omega)$, it is a simple matter to deduce that the homogenized equations (3.4), or equivalently (3.12), specialize in this case to

$$\begin{cases} \dfrac{\partial}{\partial X_k}\left[-\widetilde{\varepsilon}^{\star}_{kl}(\omega)\dfrac{\partial\widetilde{\varphi}}{\partial X_l}(\mathbf{X},\omega)\right]=0, \quad \mathbf{X}\in\Omega \\ \widetilde{\varphi}(\mathbf{X},\omega)=\widetilde{\phi}(\mathbf{X},\omega), \quad \mathbf{X}\in\partial\Omega \end{cases} \tag{4.2}$$

with

$$\begin{aligned} \widetilde{\varepsilon}^{\star}_{kl}(\omega)=\widetilde{\varepsilon}^{*}_{kl}(\omega)+\alpha^{*}_{kl}(\omega) &= \int_Y \left\{\widetilde{\varepsilon}_{kp}\left(\mathbf{y},\omega\right)\left(\delta_{lp}+\frac{\partial\breve{\chi}_l}{\partial y_p}(\mathbf{y},\omega)\right)+y_k g_l(\mathbf{y},\omega)\right\}\,\mathrm{d}\mathbf{y} \\ &= \int_Y \left\{\widetilde{\varepsilon}_{kp}\left(\mathbf{y},\omega\right)\left(\delta_{lp}-\frac{\partial\chi_l}{\partial y_p}(\mathbf{y},\omega)\right)+\left(y_k-\chi_k(\mathbf{y},\omega)\right)g_l(\mathbf{y},\omega)\right\}\,\mathrm{d}\mathbf{y}, \end{aligned} \tag{4.3}$$

where, for later convenience, the notation $\breve{\chi}_l(\mathbf{y},\omega)=\Theta_l(\mathbf{y},\omega)-\chi_l(\mathbf{y},\omega)$ has been introduced and where it is recalled that $\chi_l(\mathbf{y},\omega)$ and $\Theta_l(\mathbf{y},\omega)$ are the Y-periodic functions defined by the PDEs (3.2) and (3.3). The following two remarks are in order:

i. Physical interpretation of the homogenized equations (4.2). Equations (4.2) correspond to the governing equations for the complex electric potential $\widetilde{\varphi}(\mathbf{X},\omega)$ within a *homogeneous* dielectric medium, with effective complex permittivity tensor $\widetilde{\boldsymbol{\varepsilon}}^{\star}(\omega)$, that is subjected to Dirichlet boundary conditions.

Thus, in stark contrast to the results (3.4) and (3.12) obtained for passive charges in the previous chapter, neither an effective complex space-charge density nor a pre-polarization appear in the homogenized equations (4.2). Instead, the effect of the presence of space charges shows up in the effective complex permittivity tensor $\widetilde{\boldsymbol{\varepsilon}}^{\star}(\omega)$.

On the other hand, similar to the results (3.4) and (3.12) for passive charges, it is plain from (4.2) that the macro-variables for the complex electric field and complex electric displacement are given by

$$\widetilde{E}_k(\mathbf{X},\omega)\doteq-\frac{\partial\widetilde{\varphi}}{\partial X_k}(\mathbf{X},\omega) \qquad \text{and} \qquad \widetilde{D}_k(\mathbf{X},\omega)\doteq-\widetilde{\varepsilon}^{\star}_{kl}(\omega)\frac{\partial\widetilde{\varphi}}{\partial X_l}(\mathbf{X},\omega),$$

which in terms of their local counterparts (3.8) and (3.9) read as

$$\widetilde{E}_k(\mathbf{X},\omega) = \int_Y \widetilde{E}_k^{(0)}\left(\mathbf{X},\mathbf{y},\omega\right) \mathrm{d}\mathbf{y}$$

and

$$\begin{aligned}\widetilde{D}_k(\mathbf{X},\omega) &= \int_Y \widetilde{D}_k^{(0)}\left(\mathbf{X},\mathbf{y},\omega\right) \mathrm{d}\mathbf{y} - \left(\int_Y y_k g_l(\mathbf{y},\omega)\mathrm{d}\mathbf{y}\right) \frac{\partial\widetilde{\varphi}}{\partial X_l}(\mathbf{X},\omega) \\ &= \int_{\partial Y} y_k \widetilde{D}_l^{(0)}\left(\mathbf{X},\mathbf{y},\omega\right) n_l \mathrm{d}\mathbf{y}.\end{aligned}$$

ii. The effective complex permittivity tensor $\widetilde{\boldsymbol{\varepsilon}}^{\star}(\omega)$. The effective complex permittivity tensor (4.3) in the homogenized equations (4.2) is different from the standard result $(3.5)_1$ that emerged in the homogenized equations (3.4) for the case of passive charges. Specifically, while it is also independent of the domain Ω occupied by the dielectric and the boundary conditions on $\partial\Omega$, the effective tensor (4.3) does depend strongly on the presence of space charges via the constitutive function $\mathbf{g}(\delta^{-1}\mathbf{X},\omega)$, which, once more, controls the local distribution of the space charges at the length scale of the microstructure. Because of this dependence, the effective tensor (4.3) is *not* necessarily symmetric, *nor* positive definite for the cases when is symmetric. Moreover, because they are proportional to the constitutive function $\mathbf{g}(\delta^{-1}\mathbf{X},\omega)$, the real and imaginary parts of the components of $\widetilde{\boldsymbol{\varepsilon}}^{\star}(\omega)$ can be made to achieve arbitrarily large positive or negative values. All these features have deep physical implications as they indicate that shrewd manipulation of space charges in dielectrics provides a promising path towards the design of materials with exceptional macroscopic properties ranging from materials with unusually large permittivities to metamaterials featuring negative permittivity.

We close this remark by noticing from the two different but equivalent formulas (4.3) that the effective complex permittivity tensor $\widetilde{\boldsymbol{\varepsilon}}^{\star}(\omega)$ can be obtained either from knowledge solely of the Y–periodic function $\chi_l(\mathbf{y},\omega)$ without having to determine $\Theta_l(\mathbf{y},\omega)$ or from knowledge of the Y–periodic function $\breve{\chi}_l(\mathbf{y},\omega) = \Theta_l(\mathbf{y},\omega) - \chi_l(\mathbf{y},\omega)$, which is

solution of the additive combination of (3.2) and (3.3), namely,

$$\begin{cases} \dfrac{\partial}{\partial y_k}\left[\widetilde{\varepsilon}_{km}\left(\mathbf{y},\omega\right)\left(\delta_{ml}+\dfrac{\partial \breve{\chi}_l}{\partial y_m}(\mathbf{y},\omega)\right)\right]=g_l\left(\mathbf{y},\omega\right), \quad \mathbf{y}\in Y \\ \int_Y \breve{\chi}_l(\mathbf{y},\omega)\mathrm{d}\mathbf{y}=0 \end{cases}.$$

CHAPTER 5

SPECIALIZATION OF THE RESULT FOR $\widetilde{\boldsymbol{\varepsilon}}^{\star}(\omega)$ TO A CLASS OF ISOTROPIC PARTICULATE COMPOSITES CONTAINING ACTIVE CHARGES

The homogenized equations put forth in Chapter 4, much like those introduced in Chapter 3, apply to dielectric composite materials with arbitrary local complex permittivity $\widetilde{\boldsymbol{\varepsilon}}(\delta^{-1}\mathbf{X},\omega)$ and also to arbitrary local complex space charge function $\mathbf{g}(\delta^{-1}\mathbf{X},\omega)$ subject to the condition of local charge neutrality (2.5). In preparation for the comparisons with experiments on polymer nanoparticulate composites presented below, we spell out next the specialization in $\mathbb{R}^3$ of the result (4.3) for the effective complex permittivity tensor $\widetilde{\boldsymbol{\varepsilon}}^{\star}(\omega)$ in the homogenized equations (4.2) to a class of *isotropic particulate* composite materials containing active charges.

Specifically, we consider three-phase dielectrics exhibiting overall isotropic behavior that are made up of a $\mathtt{m}$atrix filled with spherical $\mathtt{p}$articles bonded to the matrix through constant-thickness $\mathtt{i}$nterphases containing active space charges. The matrix, particles, and interphases all feature different homogeneous isotropic complex permittivities, $\widetilde{\varepsilon}_{\mathtt{m}}(\omega)$, $\widetilde{\varepsilon}_{\mathtt{p}}(\omega)$, and $\widetilde{\varepsilon}_{\mathtt{i}}(\omega)$. The local complex permittivity of this class of dielectrics can thus be expediently written in the form

$$\widetilde{\boldsymbol{\varepsilon}}(\mathbf{y},\omega)=\widetilde{\varepsilon}(\mathbf{y},\omega)\mathbf{I}\qquad\text{with}\qquad\widetilde{\varepsilon}(\mathbf{y},\omega)=(1-\theta_{\mathtt{p}}(\mathbf{y})-\theta_{\mathtt{i}}(\mathbf{y}))\widetilde{\varepsilon}_{\mathtt{m}}(\omega)+\theta_{\mathtt{p}}(\mathbf{y})\widetilde{\varepsilon}_{\mathtt{p}}(\omega)+\theta_{\mathtt{i}}(\mathbf{y})\widetilde{\varepsilon}_{\mathtt{i}}(\omega),\tag{5.1}$$

where $\mathbf{I}$ denotes the identity second-order tensor while $\theta_{\mathtt{p}}(\mathbf{y})$ and $\theta_{\mathtt{i}}(\mathbf{y})$ stand for, respectively, the indicator functions of the spatial regions occupied by the particles and the surrounding interphases. Following Lopez-Pamies et al. (2014), the density $\widetilde{Q}^{\delta}(\mathbf{X},\omega)$ of the active space charges within the interphases is taken to be characterized by the functions (4.1) and

$$\mathbf{g}(\mathbf{y},\omega)=\theta_{\mathtt{i}}(\mathbf{y})\mathfrak{q}_{\mathtt{i}}(\mathtt{R}_{\mathtt{p}},\omega)\frac{\mathbf{y}-\mathbf{y}_{\mathtt{p}}}{|\mathbf{y}-\mathbf{y}_{\mathtt{p}}|}\qquad\text{with}\qquad\mathfrak{q}_{\mathtt{i}}(\mathtt{R}_{\mathtt{p}},\omega)=\frac{q_{\mathtt{i}}(\omega)}{\mathtt{R}_{\mathtt{p}}}.\tag{5.2}$$

Here, $\mathbf{y}_{\mathtt{p}}$ and $\mathtt{R}_{\mathtt{p}}$ stand for the centers and the *normalized* — with respect to the microscopic length scale δ — radii of however many particles are selected to be contained in the unit cell $Y = (0,1)^3$, while $q_{\mathtt{i}}(\omega) \in \mathbb{C}$ is any function of choice (with unit F/m, like $\widetilde{\varepsilon}(\mathbf{y},\omega)$) of the angular frequency ω. Note that the required condition of local charge neutrality (2.5) is indeed satisfied by the form (5.2) and that its dependence on $\mathtt{R}_{\mathtt{p}}$ implies that smaller particles feature a larger density of active charges within their surrounding interphases. It is also fitting to remark that the functional forms (4.1) together with (5.2), while phenomenological, are consistent with the interphasial charge distributions found in isotropic suspensions of dielectric spherical particles in electrolytic solutions featuring enhanced macroscopic permittivities; see, e.g., Schwan et al. (1962) and Chew and Sen (1982).

Granted the restriction to dielectrics with overall isotropic behavior, the local complex permittivity (5.1), and the local space charge functions (4.1) and (5.2), it is a simple matter to deduce that the result (4.3) for the effective complex permittivity tensor specializes to

$$\widetilde{\boldsymbol{\varepsilon}}^{\star}(\omega) = \widetilde{\varepsilon}^{\star}(\omega)\mathbf{I} \tag{5.3}$$

with

$$\begin{aligned} \widetilde{\varepsilon}^{\star}(\omega) = \int_Y \left\{ \widetilde{\varepsilon}(\mathbf{y},\omega)\left(1 + \frac{\partial \breve{\chi}_k}{\partial y_k}(\mathbf{y},\omega)\right) + \theta_{\mathtt{i}}(\mathbf{y}) q_{\mathtt{i}}(\omega) \frac{y_k (y_k - y_{\mathtt{p}_k})}{\mathtt{R}_{\mathtt{p}} |\mathbf{y} - \mathbf{y}_{\mathtt{p}}|} \right\} \mathrm{d}\mathbf{y} \\ k = 1,2,3; \text{no summation}, \end{aligned} \tag{5.4}$$

where $\breve{\chi}_k(\mathbf{y},\omega)$ is implicitly defined as the solution of the PDE

$$\begin{cases} \dfrac{\partial}{\partial y_l}\left[\widetilde{\varepsilon}(\mathbf{y},\omega)\left(\delta_{kl} + \dfrac{\partial \breve{\chi}_k}{\partial y_l}(\mathbf{y},\omega)\right)\right] = \theta_{\mathtt{i}}(\mathbf{y}) q_{\mathtt{i}}(\omega) \dfrac{y_k - y_{\mathtt{p}_k}}{\mathtt{R}_{\mathtt{p}} |\mathbf{y} - \mathbf{y}_{\mathtt{p}}|}, \quad \mathbf{y} \in Y \\ \int_Y \breve{\chi}_k(\mathbf{y},\omega) \mathrm{d}\mathbf{y} = 0 \end{cases} . \tag{5.5}$$

In the next three sections, we further specialize the result (5.3)–(5.4) to two types of spatial distributions and size dispersions of the spherical filler particles, and spell out some specific constitutive models for the complex permittivities of the matrix, particles, and interphases, $\widetilde{\varepsilon}_{\mathtt{m}}(\omega)$, $\widetilde{\varepsilon}_{\mathtt{p}}(\omega)$, $\widetilde{\varepsilon}_{\mathtt{i}}(\omega)$, as well as for the complex space charge function, $q_{\mathtt{i}}(\omega)$.

5.1 A simple cubic distribution of spherical particles of monodisperse size

The most basic type of arrangement of spherical particles surrounded by constant-thickness interphases that leads to an overall isotropic behavior is arguably that of a simple cubic distribution of particles of monodisperse size. For this type of microstructures, the indicator functions $\theta_{\mathtt{p}}(\mathbf{y})$ and $\theta_{\mathtt{i}}(\mathbf{y})$ in the local complex permittivity (5.1) take the simple form

$$\theta_{\mathtt{p}}(\mathbf{y}) = \begin{cases} 1 \text{ if } |\mathbf{y}-\mathbf{y}_{\mathtt{p}}| < \mathtt{R}_{\mathtt{p}} \\ 0 \text{ otherwise} \end{cases} \quad \text{and} \quad \theta_{\mathtt{i}}(\mathbf{y}) = \begin{cases} 1 \text{ if } \mathtt{R}_{\mathtt{p}} < |\mathbf{y}-\mathbf{y}_{\mathtt{p}}| < \mathtt{R}_{\mathtt{p}} + \mathtt{t}_{\mathtt{i}} \\ 0 \text{ otherwise} \end{cases}, \tag{5.6}$$

where, for definiteness, $\mathbf{y}_{\mathtt{p}} = (1/2, 1/2, 1/2)$, and where $\mathtt{R}_{\mathtt{p}} = (3c_{\mathtt{p}}/4\pi)^{1/3}$, $\mathtt{t}_{\mathtt{i}} = (3(c_{\mathtt{p}} + c_{\mathtt{i}})/4\pi)^{1/3} - (3c_{\mathtt{p}}/4\pi)^{1/3}$ with $c_{\mathtt{p}} = \int_Y \theta_{\mathtt{p}}(\mathbf{y})\mathrm{d}\mathbf{y}$ and $c_{\mathtt{i}} = \int_Y \theta_{\mathtt{i}}(\mathbf{y})\mathrm{d}\mathbf{y}$ denoting the volume fractions of particles and interphases in the dielectric. Figure 5.1 shows a schematic of the defining unit cell Y.

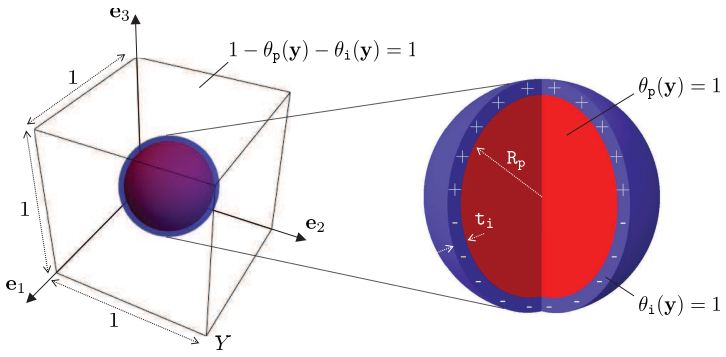

Figure 5.1: Schematic of the unit cell $Y = (0,1)^3$ illustrating the simple cubic distribution of monodisperse spherical particles and the surrounding constant-thickness interphases containing the space charges.

For the case of indicator functions (5.6), the PDE (5.5) does not generally admit explicit solutions, but it is straightforward to generate numerical solutions for it, for instance, via the finite element method. In turn, once such numerical solutions for the field $\breve{\chi}_k(\mathbf{y},\omega)$ have been generated, the integral (5.4) can be evaluated by means of a quadrature rule to finally determine the resulting effective complex permittivity tensor (5.3). In the next section, we

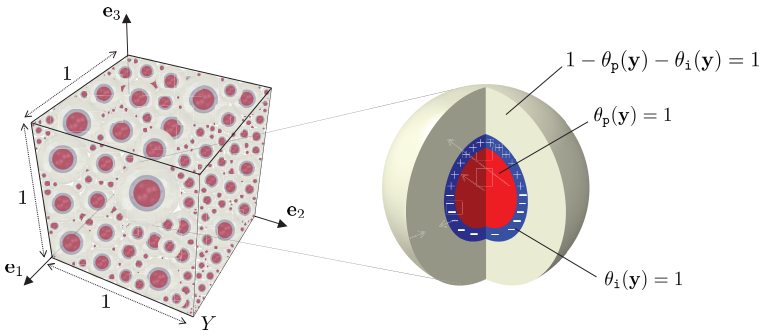

Figure 5.2: Schematic of the unit cell $Y=(0,1)^3$ replete with an assemblage of homothetic multicoated spheres. The filler spherical particles and their surrounding constant-thickness interphases containing the space charges are randomly distributed in space and polydisperse in size.

shall present a sample of such numerical solutions.

5.2 A random isotropic distribution of spherical particles of polydisperse sizes

The second type of arrangement of spherical particles surrounded by constant-thickness interphases that we consider is that of an assemblage of homothetic multicoated spheres made up of a core (the particle), an inner shell (the interphase), and an outer shell (the matrix), that fills in the entire unit cell $Y=(0,1)^3$; see, e.g., Hashin (1962), Chapter 7 in Milton (2002), Chapter 25 in Tartar (2009) for a historical account and for various perspectives on coated sphere assemblages in the absence of space charges and Lopez-Pamies et al. (2014) for a neutral-inclusion perspective of coated sphere assemblages containing interphasial space charges. In such microstructures, there are infinitely many particles in the unit cell and these have random centers $\mathbf{y}_{\mathtt{p}}\in Y$ and polydisperse normalized radii in the range $0<\mathtt{R}_{\mathtt{p}}<1/2-(3(c_{\mathtt{p}}+c_{\mathtt{i}})/4\pi)^{1/3}+(3c_{\mathtt{p}}/4\pi)^{1/3}$, where, again, $c_{\mathtt{p}}$ and $c_{\mathtt{i}}$ stand for the volume fractions of particles and interphases in the dielectric. Accordingly, the indicator functions $\theta_{\mathtt{p}}(\mathbf{y})$ and $\theta_{\mathtt{i}}(\mathbf{y})$ in the local complex permittivity (5.1) are the union of indicator functions of the form (5.6) for all the homothetic multicoated spheres in the assemblage. Figure 5.2 shows a schematic of the defining unit cell Y.

Now, thanks to the choice $(5.2)_2$ for $\mathfrak{q}_{\mathtt{i}}(\mathtt{R}_{\mathtt{p}},\omega)$ in the complex space charge function $\mathbf{g}(\mathbf{y},\omega)$,

the homothetic multicoated spheres described above can be shown to behave as neutral inclusions and so, by leveraging the same neutral-inclusion derivation introduced in Lopez-Pamies et al. (2014), the PDE (5.5) can be solved in closed form and the integral (5.4) can in turn be evaluated explicitly. Omitting the argument ω for notational simplicity, the result reads as follows:

$$\widetilde{\varepsilon}^{\star} = \widetilde{\varepsilon}_{\mathtt{m}} + \frac{3\widetilde{\varepsilon}_{\mathtt{m}}(c_{\mathtt{i}}+c_{\mathtt{p}})\left[c_{\mathtt{i}}(\widetilde{\varepsilon}_{\mathtt{i}}-\widetilde{\varepsilon}_{\mathtt{m}})(2\widetilde{\varepsilon}_{\mathtt{i}}+\widetilde{\varepsilon}_{\mathtt{p}})+3c_{\mathtt{p}}\widetilde{\varepsilon}_{\mathtt{i}}(\widetilde{\varepsilon}_{\mathtt{p}}-\widetilde{\varepsilon}_{\mathtt{m}})\right]}{\widetilde{\varepsilon}_{\mathtt{p}}\left[\widetilde{\varepsilon}_{\mathtt{i}}(1-c_{\mathtt{i}}-c_{\mathtt{p}})(c_{\mathtt{i}}+3c_{\mathtt{p}})+c_{\mathtt{i}}\widetilde{\varepsilon}_{\mathtt{m}}(c_{\mathtt{i}}+c_{\mathtt{p}}+2)\right]+\widetilde{\varepsilon}_{\mathtt{i}}\left[\widetilde{\varepsilon}_{\mathtt{m}}(c_{\mathtt{i}}+c_{\mathtt{p}}+2)(2c_{\mathtt{i}}+3c_{\mathtt{p}})+2c_{\mathtt{i}}\widetilde{\varepsilon}_{\mathtt{i}}(1-c_{\mathtt{i}}-c_{\mathtt{p}})\right]}$$
$$+\frac{3\widetilde{\varepsilon}_{\mathtt{m}}c_{\mathtt{p}}(c_{\mathtt{i}}+c_{\mathtt{p}})\left(3\left(1+\dfrac{c_{\mathtt{i}}}{c_{\mathtt{p}}}\right)^{1/3}(2\widetilde{\varepsilon}_{\mathtt{i}}-\widetilde{\varepsilon}_{\mathtt{p}})+\dfrac{c_{\mathtt{i}}}{c_{\mathtt{p}}}\left(1+\dfrac{c_{\mathtt{i}}}{c_{\mathtt{p}}}\right)^{1/3}(2\widetilde{\varepsilon}_{\mathtt{i}}+\widetilde{\varepsilon}_{\mathtt{p}})+3(\widetilde{\varepsilon}_{\mathtt{p}}-2\widetilde{\varepsilon}_{\mathtt{i}})\right)q_{\mathtt{i}}}{4\widetilde{\varepsilon}_{\mathtt{p}}\left[\widetilde{\varepsilon}_{\mathtt{i}}(1-c_{\mathtt{i}}-c_{\mathtt{p}})(c_{\mathtt{i}}+3c_{\mathtt{p}})+c_{\mathtt{i}}\widetilde{\varepsilon}_{\mathtt{m}}(c_{\mathtt{i}}+c_{\mathtt{p}}+2)\right]+4\widetilde{\varepsilon}_{\mathtt{i}}\left[\widetilde{\varepsilon}_{\mathtt{m}}(c_{\mathtt{i}}+c_{\mathtt{p}}+2)(2c_{\mathtt{i}}+3c_{\mathtt{p}})+2c_{\mathtt{i}}\widetilde{\varepsilon}_{\mathtt{i}}(1-c_{\mathtt{i}}-c_{\mathtt{p}})\right]}. \tag{5.7}$$

We remark that the simple explicit result (5.7) is nothing more than the formula[1] (10) in Lopez-Pamies et al. (2014) transcribed to the realm of complex frequency-dependent permittivities.

5.3 Constitutive models for $\widetilde{\varepsilon}_{\mathtt{m}}(\omega)$, $\widetilde{\varepsilon}_{\mathtt{p}}(\omega)$, $\widetilde{\varepsilon}_{\mathtt{i}}(\omega)$, and $q_{\mathtt{i}}(\omega)$

The preceding results are valid for any choice of isotropic complex permittivities $\widetilde{\varepsilon}_{\mathtt{m}}(\omega)$, $\widetilde{\varepsilon}_{\mathtt{p}}(\omega)$, $\widetilde{\varepsilon}_{\mathtt{i}}(\omega)$ and any choice of complex space charge function $q_{\mathtt{i}}(\omega)$. Out of these, $\widetilde{\varepsilon}_{\mathtt{m}}(\omega)$ and $\widetilde{\varepsilon}_{\mathtt{p}}(\omega)$ are directly measurable from standard spectroscopy experiments. On the other hand, as already alluded to above, $\widetilde{\varepsilon}_{\mathtt{i}}(\omega)$ and $q_{\mathtt{i}}(\omega)$ are difficult to have access to experimentally, even indirectly, due to the inherent nanometer scale of interphases.

In the comparisons with the experiments that follow, we will make use of direct experimental data for $\widetilde{\varepsilon}_{\mathtt{m}}(\omega)$ and $\widetilde{\varepsilon}_{\mathtt{p}}(\omega)$ whenever available. In the absence of direct experimental data over the complete range of frequencies of interest, we will make use of the well-established five-parameter Havriliak-Negami model, precisely,

$$\widetilde{\varepsilon}_{\mathtt{m}}(\omega) = \varepsilon_{\mathtt{m}_\infty} + \frac{\varepsilon_{\mathtt{m}_0}-\varepsilon_{\mathtt{m}_\infty}}{(1+(i\omega\tau_{\mathtt{m}})^{\alpha_{\mathtt{m}}})^{\beta_{\mathtt{m}}}} \qquad \text{and} \qquad \widetilde{\varepsilon}_{\mathtt{p}}(\omega) = \varepsilon_{\mathtt{p}_\infty} + \frac{\varepsilon_{\mathtt{p}_0}-\varepsilon_{\mathtt{p}_\infty}}{(1+(i\omega\tau_{\mathtt{p}})^{\alpha_{\mathtt{p}}})^{\beta_{\mathtt{p}}}}, \tag{5.8}$$

[1] The third term in the formula (10) reported in Lopez-Pamies et al. (2014) contains typographical errors which are corrected in (5.7).

where $\varepsilon_{\mathtt{m}_\infty}, \varepsilon_{\mathtt{m}_0} \geq 0$ denote, respectively, the limiting values of the permittivity of the matrix at high and low frequencies, while the material constants $\tau_{\mathtt{m}} \geq 0$, $\alpha_{\mathtt{m}} > 0$, and $0 < \beta_{\mathtt{m}} \leq 1/\alpha_{\mathtt{m}}$ describe its relaxation behavior (*idem* for $\varepsilon_{\mathtt{p}_\infty}$, $\varepsilon_{\mathtt{p}_0}$, $\tau_{\mathtt{p}}$, $\alpha_{\mathtt{p}}$, and $\beta_{\mathtt{p}}$). We recall that the Havriliak-Negami model is a combination of the Cole-Cole ($\beta_{\mathtt{m}} = 1$) and the Davidson-Cole ($\alpha_{\mathtt{m}} = 1$) models — which in turn are generalizations of the basic Debye ($\alpha_{\mathtt{m}} = \beta_{\mathtt{m}} = 1$) model — that has been shown to be well descriptive of a broad spectrum of materials, including a wide variety of polymers; see Debye (1929), Cole and Cole (1941), Davidson and Cole (1951), Havriliak and Negami (1966) for the derivation of these models and their comparisons with a wide range of experimental results, see, e.g., also Garrappa et al. (2016) for a recent description and discussion of these models in the time domain.

For the complex permittivity of the interphases $\widetilde{\varepsilon}_{\mathtt{i}}(\omega)$, we will make use of one of the following three limiting models:

$$\widetilde{\varepsilon}_{\mathtt{i}}(\omega) = \widetilde{\varepsilon}_{\mathtt{m}}(\omega) \qquad \text{or} \qquad \widetilde{\varepsilon}_{\mathtt{i}}(\omega) = \varepsilon_0 + i\frac{\sigma_{\mathtt{i}}}{\omega} \quad \text{with} \quad \begin{cases} \sigma_{\mathtt{i}} = +\infty \\ \text{or} \\ \sigma_{\mathtt{i}} = 0 \end{cases} . \tag{5.9}$$

The choice $(5.9)_1$ corresponds to the limiting case when the dielectric behavior of the interphases is identical to that of the matrix, in other words, when there are no interphases. The choice $(5.9)_2$ with $\sigma_{\mathtt{i}} = +\infty$ corresponds to the case when the interphases are perfect conductors. On the other hand, the choice $(5.9)_2$ with $\sigma_{\mathtt{i}} = 0$ corresponds to the opposite limiting case when the interphases are perfect dielectrics featuring the permittivity of vacuum, in other words, when the interphases are vacuous.

Finally, for the complex space charge function $q_{\mathtt{i}}(\omega)$, we will also make use of a Havriliak-Negami-type model. We write

$$q_{\mathtt{i}}(\omega) = q_\infty + \frac{q_0 - q_\infty}{\left(1 + (i\omega\tau_{q_{\mathtt{i}}})^{\alpha_{q_{\mathtt{i}}}}\right)^{\beta_{q_{\mathtt{i}}}}}, \tag{5.10}$$

where we recall that $q_{\mathtt{i}}(\omega)$ has units of F/m, like the complex permittivities $\widetilde{\varepsilon}_{\mathtt{m}}(\omega)$, $\widetilde{\varepsilon}_{\mathtt{p}}(\omega)$, and $\widetilde{\varepsilon}_{\mathtt{i}}(\omega)$.

CHAPTER 6

APPLICATION TO POLYMER NANOPARTICULATE COMPOSITES AND FINAL COMMENTS

In the sequel, we deploy the foregoing theoretical framework for the effective complex permittivity $\widetilde{\boldsymbol{\varepsilon}}^{\star}(\omega)$ to compare with and examine three representative sets of experimental data available in the literature for polymer nanoparticulate composites. The objective is to illustrate the use of the proposed homogenization results and to showcase their ability not only to describe the macroscopic response of emerging polymer nanoparticulate composites featuring extreme dielectric behaviors in terms of space charges varying a the length scale of their filler nanoparticles but also, and more critically, to point to the manipulation of space charges as a promising strategy for the bottom-up design of materials with exceptional macroscopic properties.

6.1 The experiments of Huang et al. (2005) on polyurethane filled with o-CuPC nanoparticles

We begin by examining the experimental results of Huang et al. (2005) for the dielectric response at room temperature of a polyurethane (PU) polymer isotropically filled with semi-conducting copper phthalocyanine oligomer (o-CuPc) nanoparticles of roughly spherical shape, coated with a polyacrylic acid, at volume fraction $c_{\mathrm{p}} = 0.073$ under a uniform alternating electric field with frequencies $f = \omega/2\pi$ ranging from 20 Hz to 1 MHz. These results are reproduced (solid lines) in Fig. 6.1 for the real $\varepsilon^{\star\prime}(\omega)$ and imaginary $\varepsilon^{\star\prime\prime}(\omega)$ parts of the effective complex permittivity $\widetilde{\varepsilon}^{\star}(\omega) = \varepsilon^{\star\prime}(\omega) - i\varepsilon^{\star\prime\prime}(\omega)$ of the composite, normalized by the permittivity of vacuum ε_0, as functions of the frequency f. To aid in the discussion, Fig. 6.1 includes the corresponding response (dashed lines) of the unfilled PU polymer, which was also reported by Huang et al. (2005).

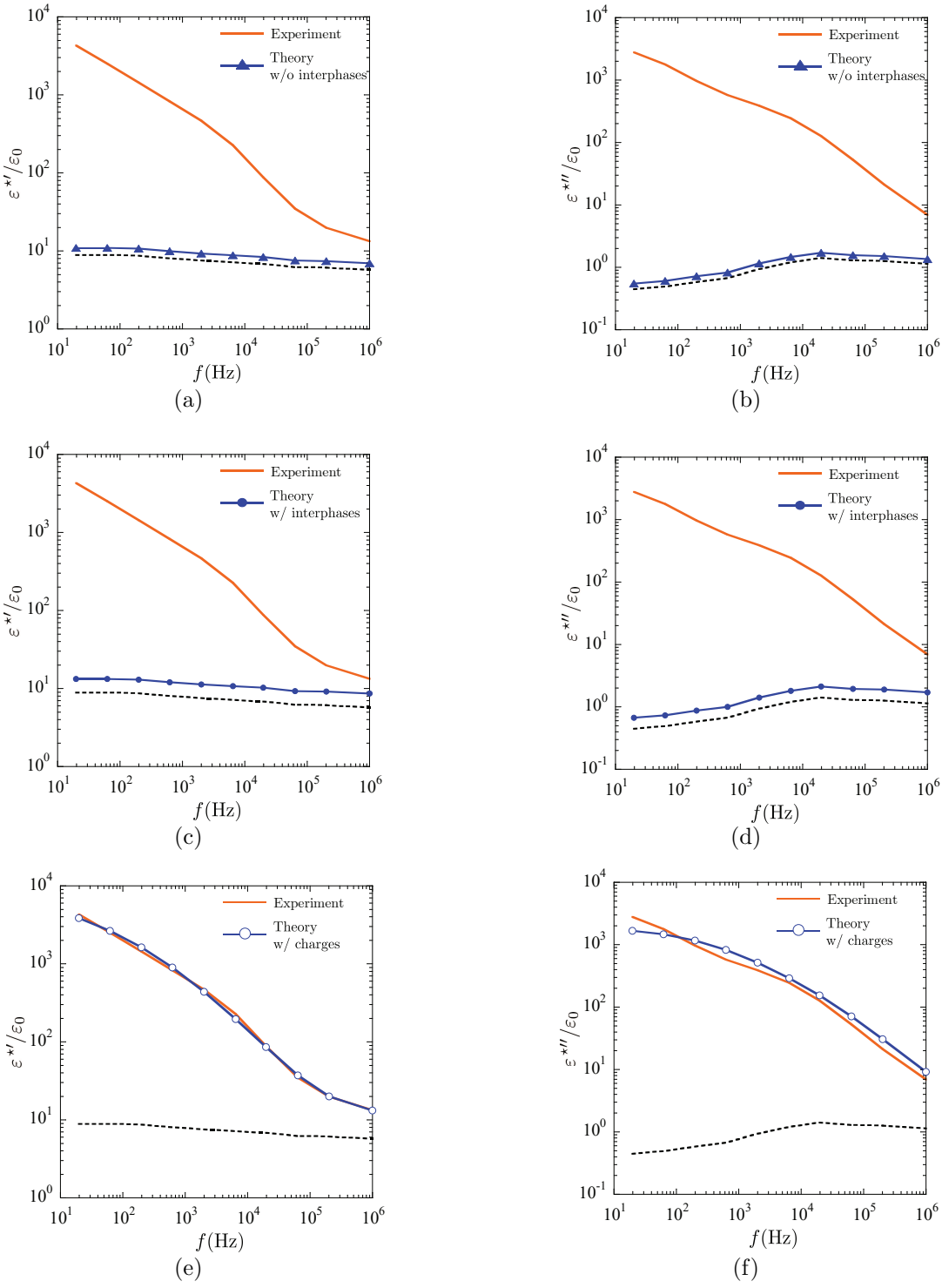

Figure 6.1: Comparisons between the experimental results (solid lines) of Huang et al. (2005) for a PU polymer filled with o-CuPC nanoparticles and the proposed theoretical results: (a)-(b) without interphases (triangles), (c)-(d) with interphases (solid circles), and (e)-(f) with space charges (empty circles). The comparisons are shown for the real and complex parts of the effective complex permittivity $\widetilde{\varepsilon}^{\star}(\omega) = \varepsilon^{\star\prime}(\omega) - i\varepsilon^{\star\prime\prime}(\omega)$, normalized by the permittivity of vacuum ε_0, as functions of the frequency $f = \omega/2\pi$ of the applied electric field. For further comparison, all the plots include the corresponding experimentally measured response (dashed lines) of the unfilled PU polymer.

First, Figs. 6.1(a) and (b) confront the experimental data to the theoretical results for the basic case when there are no interphases and no space charges. Specifically, the theoretical results presented in Figs. 6.1(a) and (b) correspond to the effective complex permittivity (5.7) for a random isotropic distribution of polydisperse spherical particles with $c_{\mathtt{p}} = 0.073$, $c_{\mathtt{i}} = 0$, $q_i(\omega) = 0$ where the complex permittivities for the PU polymer $\widetilde{\varepsilon}_{\mathtt{m}}(\omega)$ and for the o-CuPC nanoparticles $\widetilde{\varepsilon}_{\mathtt{p}}(\omega)$ take the experimental values reported by Huang et al. (2005) and Wang et al. (2005), respectively. The primary and immediate observation from these figures is that the basic assumption of perfect bonding between the o-CuPC nanoparticles and the PU polymer is inadequate to explain the drastic enhancement — more than three orders of magnitude at low frequencies — of both the real and the imaginary parts of the complex permittivity of this nanoparticulate composite.

Figures 6.1(c) and (d) present the same type of comparisons as Figs. 6.1(a) and (b), but now the theoretical results incorporate the presence of interphases between the o-CuPC nanoparticles and the PU polymer. Given that the o-CuPC nanoparticles have an average radius of roughly 20 nm, it is reasonable to assume that they may be surrounded by interphases of about 5 nm in average thickness, which would translate into a total volume fraction of interphases of $c_{\mathtt{i}} = 0.070$; see, e.g., Qu et al. (2003) and Meddeb et al. (2019) for relevant experimental work on the measurement of the geometry of interphases. Moreover, in order to obtain the maximum enhancement possible from the presence of such interphases, it is reasonable to assume that they are perfect conductors[1]. Accordingly, the theoretical results in Figs. 6.1(c) and (d) correspond to the effective complex permittivity (5.7) with $c_{\mathtt{p}} = 0.073$, $c_{\mathtt{i}} = 0.070$, $q_i(\omega) = 0$, where, again, the complex permittivities for the PU polymer $\widetilde{\varepsilon}_{\mathtt{m}}(\omega)$ and the o-CuPC nanoparticles $\widetilde{\varepsilon}_{\mathtt{p}}(\omega)$ take the experimental values reported by Huang et al. (2005) and Wang et al. (2005), and where the interphases are perfect conductors characterized by the complex permittivity $\widetilde{\varepsilon}_{\mathtt{i}}(\omega) = \varepsilon_0 + i\sigma_{\mathtt{i}}/\omega$ with $\sigma_{\mathtt{i}} = +\infty$. From a quick glance at Figs. 6.1(c) and (d), it is plain that accounting for the presence of interphases appears, by itself, also inadequate[2] to explain the drastically enhanced response exhibited by the

[1]This is effectively equivalent to assuming alternatively that the interphases are perfect dielectrics with infinity permittivity, that is, $\widetilde{\varepsilon}_{\mathtt{i}}(\omega) = \varepsilon'_{\mathtt{i}}$ with $\varepsilon'_{\mathtt{i}} = +\infty$.

[2]Beyond the illustrative results shown in Figs. 6.1(c) and (d), the inadequacy of conducting (or high-permittivity) interphases as the mechanism of enhancement can be readily deduced by recognizing from the

composite.

Finally, Figs. 6.1(e) and (f) present the comparisons between the experimental data and the theoretical results now for the case when space charges are accounted for. Precisely, the theoretical results plotted in these figures correspond to the effective complex permittivity (5.7) with $c_{\mathtt{p}} = 0.073$, $c_{\mathtt{i}} = 0.070$, $\widetilde{\varepsilon}_{\mathtt{m}}(\omega)$ and $\widetilde{\varepsilon}_{\mathtt{p}}(\omega)$ taking, again, the experimental values reported by Huang et al. (2005) and Wang et al. (2005), where $\widetilde{\varepsilon}_{\mathtt{i}}(\omega) = \widetilde{\varepsilon}_{\mathtt{m}}(\omega)$ and the complex space charge function $q_{\mathtt{i}}(\omega)$ is given by the Havriliak-Negami-type relation (5.10) with parameters $q_0 = 1.381 \times 10^6 \varepsilon_0$, $q_\infty = 460\varepsilon_0$, $\tau_{q_{\mathtt{i}}} = 1.161 \times 10^{-3}$ s, $\alpha_{q_{\mathtt{i}}} = 0.2730$, and $\beta_{q_{\mathtt{i}}} = 3.662$. The close agreement possible between the theoretical results and the experimental data shown in Figs. 6.1(e) and (f) suggests that the presence of active space charges might indeed be the mechanism responsible for the drastically enhanced complex permittivity exhibited by this type of PU polymer filled with o-CuPC nanoparticles.

6.2 The experiments of Thakur et al. (2017) on polyetherimide filled with Al_2O_3 nanoparticles

Next, we turn to examine the experimental data of Thakur et al. (2017) for the dielectric response of a polyetherimide (PEI) polymer isotropically filled with a very small content of Al_2O_3 nanoparticles of roughly spherical shape under a uniform alternating electric field varying from 1 kHz to 1 MHz in frequency. While Thakur et al. (2017) reported data for a range of temperatures as well as for a range of sizes and small volume fractions of nanoparticles, we focus here on the case that exhibited the largest dielectric enhancement at room temperature, namely, that of a PEI polymer filled with Al_2O_3 nanoparticles of 10 nm in average radius at volume fraction $c_{\mathtt{p}} = 0.0032$. The experimental data of interest (solid lines) for the real and imaginary parts of the effective complex permittivity of this nanoparticulate composite is shown in Fig. 6.2. The corresponding response (dashed lines) of the unfilled PEI polymer, as reported by Thakur et al. (2017), is also displayed for direct

result (5.7) that its real and imaginary parts are bounded from above by $\varepsilon^{\star\prime}(\omega) \leq \varepsilon'_{\mathtt{m}}(\omega) + 3(c_{\mathtt{p}}+c_{\mathtt{i}})\varepsilon'_{\mathtt{m}}(\omega)/(1-c_{\mathtt{p}}-c_{\mathtt{i}})$ and $\varepsilon^{\star\prime\prime}(\omega) \leq \varepsilon''_{\mathtt{m}}(\omega) + 3(c_{\mathtt{p}}+c_{\mathtt{i}})\varepsilon''_{\mathtt{m}}(\omega)/(1-c_{\mathtt{p}}-c_{\mathtt{i}})$. Thus, so long as the combination of volume fractions of nanoparticles and interphases $c_{\mathtt{p}}+c_{\mathtt{i}}$ is sufficiently away from unity, the enhancement afforded by interphases is only of the same order of magnitude as the complex permittivity of the embedding polymer.

comparison.

In complete analogy with Fig. 6.1, the results are presented normalized by the permittivity of vacuum in terms of the frequency of the applied electric field. Parts (a) and (b) compare the experimental data with the theoretical results for the basic case when there are no interphases and no space charges. Parts (c) and (d) then present the comparisons with the theoretical results that account for the presence of interphases between the Al_2O_3 nanoparticles and the PEI polymer. Finally, parts (e) and (f) show the comparisons with the theoretical results that incorporate the presence of space charges.

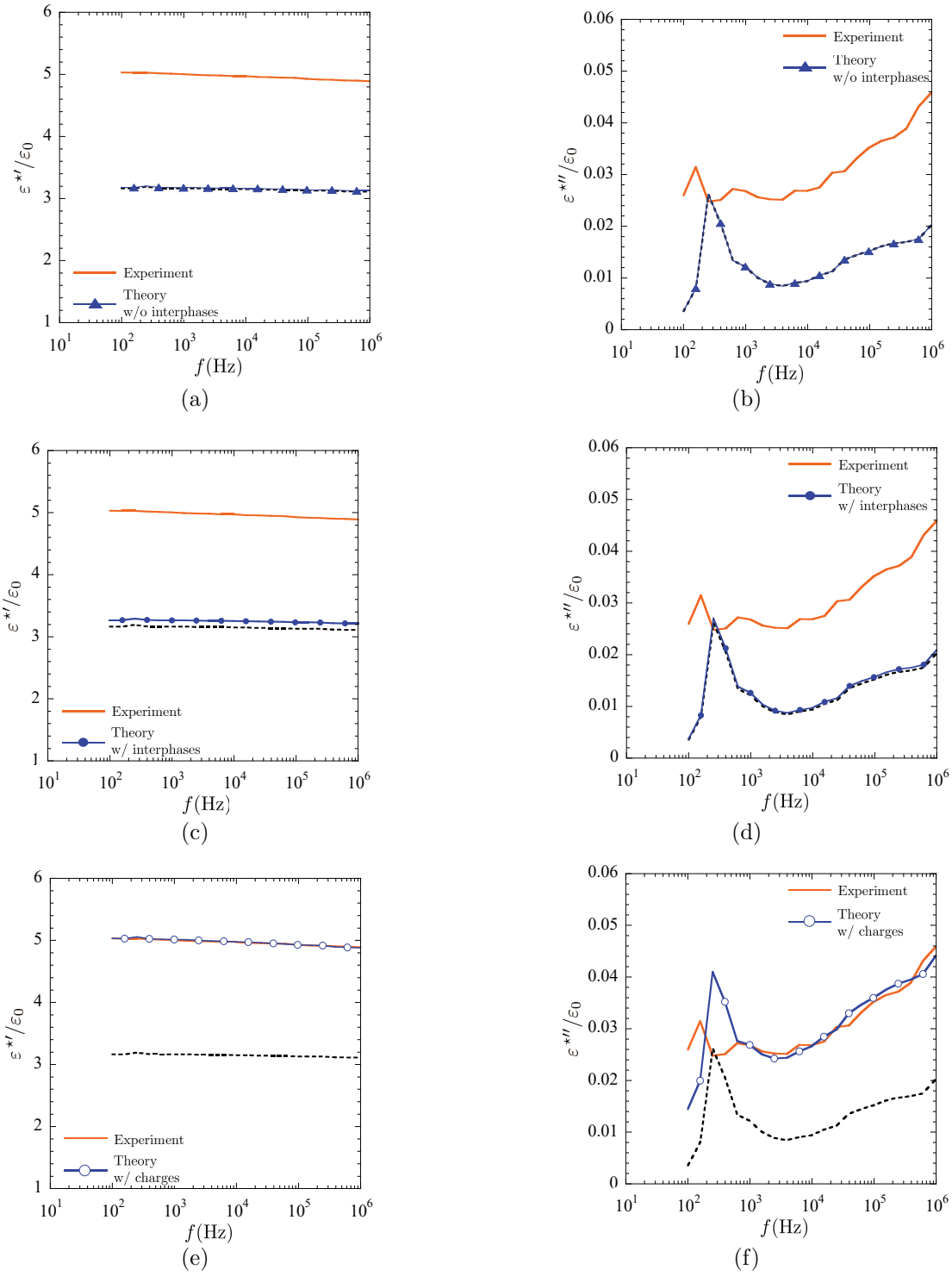

Figure 6.2: Comparisons between the experimental results (solid lines) of Thakur et al. (2017) for a PEI polymer filled with Al_2O_3 nanoparticles and the proposed theoretical results: (a)-(b) without interphases (triangles), (c)-(d) with interphases (solid circles), and (e)-(f) with space charges (empty circles). The comparisons are shown for the real and complex parts of the effective complex permittivity $\widetilde{\varepsilon}^{\star}(\omega) = \varepsilon^{\star\prime}(\omega) - i\varepsilon^{\star\prime\prime}(\omega)$, normalized by the permittivity of vacuum ε_0, as functions of the frequency $f = \omega/2\pi$ of the applied electric field. All plots include the corresponding experimentally measured response (dashed lines) of the unfilled PEI polymer.

All the theoretical results in Fig. 6.2 correspond to the formula (5.7) for the effective complex permittivity of a random isotropic distribution of polydisperse spherical particles evaluated at $c_{\mathtt{p}} = 0.0032$ with the complex permittivities for the PEI polymer $\widetilde{\varepsilon}_{\mathtt{m}}(\omega)$ and for the Al_2O_3 nanoparticles $\widetilde{\varepsilon}_{\mathtt{p}}(\omega)$ taking the experimental values reported by Thakur et al. (2017) and — since Thakur et al. (2017) did not provide the dielectric response of the Al_2O_3 nanoparticles that they used in their specimens — by Vila et al. (1998), respectively. The results in Figs. 6.2(a) and (b) correspond to the further prescription $c_{\mathtt{i}} = 0$, $q_i(\omega) = 0$, those in Figs. 6.2(c) and (d) to $c_{\mathtt{i}} = 0.0076$, $q_i(\omega) = 0$, and $\widetilde{\varepsilon}_{\mathtt{i}}(\omega) = \varepsilon_0 + i\sigma_{\mathtt{i}}/\omega$ with $\sigma_{\mathtt{i}} = +\infty$, while the results in Figs. 6.2(e) and (f) correspond to $c_{\mathtt{i}} = 0.0076$, $\widetilde{\varepsilon}_{\mathtt{i}}(\omega) = \widetilde{\varepsilon}_{\mathtt{m}}(\omega)$, and a complex space charge function $q_{\mathtt{i}}(\omega)$ given by (5.10) with parameters $q_0 = 740\varepsilon_0$, $q_\infty = 660\varepsilon_0$, $\tau_{q_{\mathtt{i}}} = 5.291 \times 10^{-8}$ s, $\alpha_{q_{\mathtt{i}}} = 0.1431$, and $\beta_{q_{\mathtt{i}}} = 0.7608$. We remark that the geometric choice of volume fraction of interphases $c_{\mathtt{i}} = 0.0076$ in Figs. 6.2(c) and (d) stems from estimating that the interphases are 5 nm in average thickness, which is a relatively large but realistic size given that the Al_2O_3 nanoparticles are, again, about 10 nm in average radius. Moreover, the constitutive choice of perfectly conducting interphases is aimed at generating the maximum enhancement possible in the dielectric response of the composite. On the other hand, the choice of parameters $q_0 = 740\varepsilon_0$, $q_\infty = 660\varepsilon_0$, $\tau_{q_{\mathtt{i}}} = 5.291 \times 10^{-8}$ s, $\alpha_{q_{\mathtt{i}}} = 0.1431$, $\beta_{q_{\mathtt{i}}} = 0.7608$ characterizing the underlying active space charges in the results presented in Figs. 6.2(e) and (f) is aimed at rendering a good agreement with the experimental data.

From all the comparisons presented in Figs. 6.2(a) through (d), it is clear that the exceptionally enhanced dielectric response of the PEI polymer filled with Al_2O_3 nanoparticles — note that the real (imaginary) part of the effective complex permittivity of this nanoparticulate composite is about 60% (120%) larger than that of the unfilled PEI polymer, in spite of the fact that the volume fraction of Al_2O_3 nanoparticles in it is extremely small, only $c_{\mathtt{p}} = 0.0032$ — cannot be explained on the basic premise of perfect bonding between the polymer and the nanoparticles. It cannot be explained either solely by the presence of interphases between the polymer and the nanoparticles. By contrast, in view of the favorable comparisons displayed in Figs. 6.2(e) and (f), space charges might be in this case too the mechanism responsible for the observed enhanced dielectric response.

6.3 The experiments of Zhang et al. (2017) on polyetherimide filled with BN nanoparticles

Again, we continue with the experimental data of Zhang et al. (2017), for the dielectric response of polyetherimide (PEI) polymer isotropically filled with a very small content of BN nanoparticles of roughly spherical shape under a uniform alternating electric field with frequencies varying from 10^{-2} Hz to 1 MHz. In Zhang et al. (2017) we focus on the case that generates the largest dielectric enhancement at room temperature, namely, that of a PEI polymer filled with BN nanoparticles of 35 nm in average radius at volume fraction $c_{\mathtt{p}} = 0.0062$. The experimental data of interest (solid lines) for the real and imaginary parts of the effective complex permittivity of this nanoparticulate composite is shown in Fig. 6.3, which includes the corresponding response (dashed lines) of the unfilled PEI polymer from Zhang et al. (2017).

Similarly, Figs. 6.3(a) and (b) compare the experimental data with the theoretical results without neither interphases nor space charges. Figs. 6.3(c) and (d) exhibit the comparisons with theoretical results that take account of the presence of interphases between the BN nanoparticles and the PEI polymer. Lastly, 6.3(e) and (f) show the comparisons with the theoretical results in the presense of space charges. Specifically, the complex permittivities for the PEI polymer $\widetilde{\varepsilon}_{\mathtt{m}}(\omega)$ and for the BN nanoparticles $\widetilde{\varepsilon}_{\mathtt{p}}(\omega)$ take the experimental values reported by Zhang et al. (2017) and Thakur et al. (2017) (here we use $\varepsilon'_p = 5, \tan\delta = 0.002$ for BN nanoparticles), respectively.

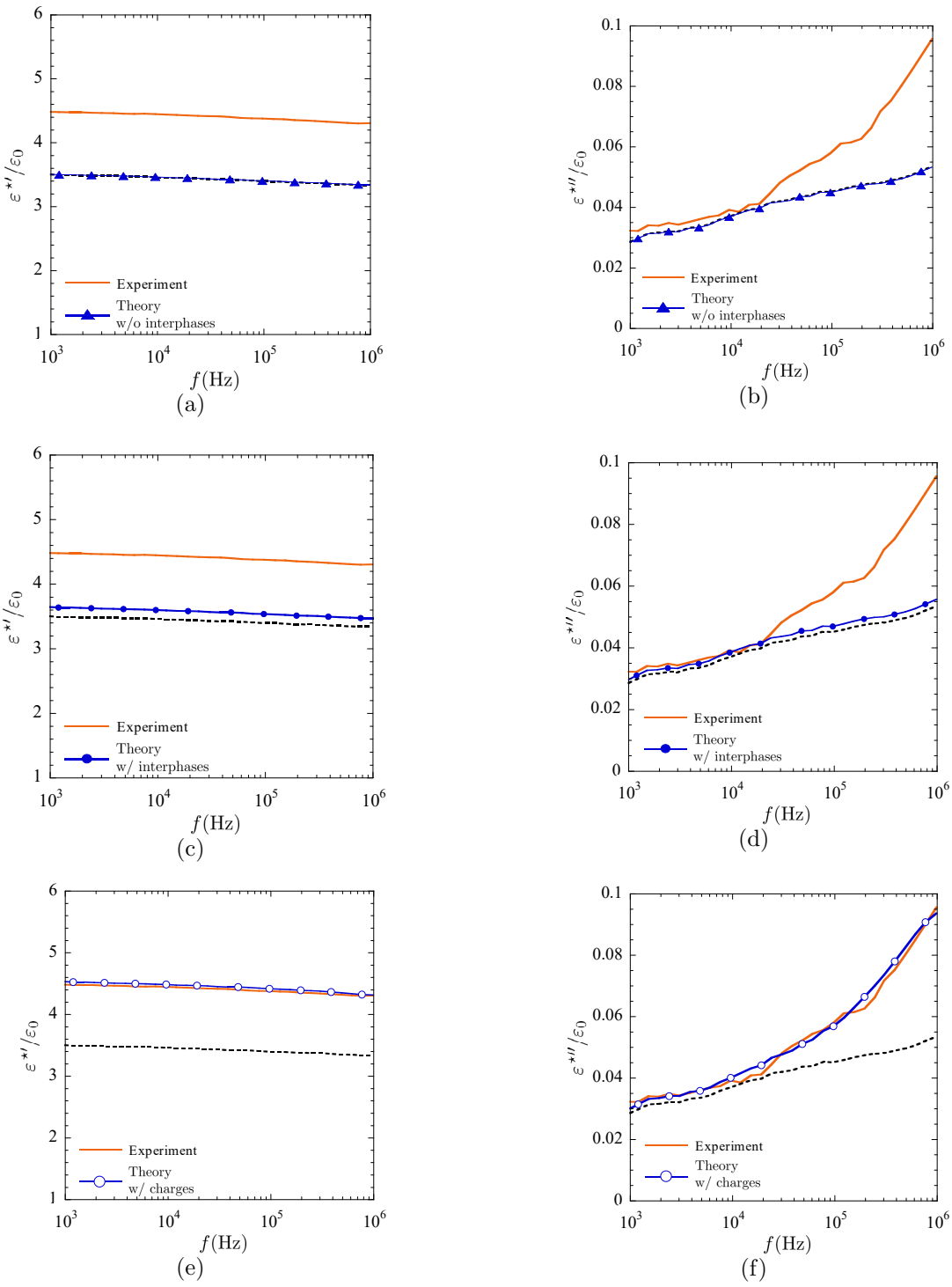

Figure 6.3: Comparisons between the experimental results (solid lines) of Zhang et al. (2017) for a PEI polymer filled with BN nanoparticles and the proposed theoretical results: (a)-(b) without interphases (triangles), (c)-(d) with interphases (solid circles), and (e)-(f) with space charges (empty circles). The comparisons are shown for the real and complex parts of the effective complex permittivity $\widetilde{\varepsilon}^{\star}(\omega) = \varepsilon^{\star\prime}(\omega) - i\varepsilon^{\star\prime\prime}(\omega)$, normalized by the permittivity of vacuum ε_0, as functions of the frequency $f = \omega/2\pi$ of the applied electric field. All plots include the corresponding experimentally measured response (dashed lines) of the unfilled PEI polymer.

The results in Figs. 6.3(a) and (b) correspond to the further prescription $c_{\mathtt{i}} = 0$, $q_i(\omega) = 0$, those in Figs. 6.3(c) and (d) to $c_{\mathtt{i}} = 0.007$, $q_i(\omega) = 0$, and $\widetilde{\varepsilon}_{\mathtt{i}}(\omega) = \varepsilon_0 + i\sigma_{\mathtt{i}}/\omega$ with $\sigma_{\mathtt{i}} = +\infty$, while the results in Figs. 6.3(e) and (f) correspond to $c_{\mathtt{i}} = 0.007$, $\widetilde{\varepsilon}_{\mathtt{i}}(\omega) = \widetilde{\varepsilon}_{\mathtt{m}}(\omega)$, and a complex space charge function $q_{\mathtt{i}}(\omega)$ from (5.10) with parameters $q_0 = 391.2\varepsilon_0$, $q_\infty = 356.2\varepsilon_0$, $\tau_{q_{\mathtt{i}}} = 1.446 \times 10^{-7}$, $\alpha_{q_{\mathtt{i}}} = 0.9$, and $\beta_{q_{\mathtt{i}}} = 0.928$. The volume fraction of interphases $c_{\mathtt{i}} = 0.007$ in Figs. 6.3(c) and (d) comes from estimating that the interphases are 15 nm in average thickness, based on the BN nanoparticles are about 35 nm in average radius. And we use perfectly conducting interphases for generating the maximum enhancement possible in the dielectric response of the composite. Meanwhile, the choice of parameters $q_0 = 391.2\varepsilon_0$, $q_\infty = 356.2\varepsilon_0$, $\tau_{q_{\mathtt{i}}} = 1.446 \times 10^{-7}$, $\alpha_{q_{\mathtt{i}}} = 0.9$, and $\beta_{q_{\mathtt{i}}} = 0.928$ characterizing the underlying active space charges in the results presented in Figs. 6.3(e) and (f) keeps us in accordance with experiments.

In general, from all the comparisons in Figs. 6.3(a) through (d), the real (imaginary) part of the effective complex permittivity of this composite is about 28% (96%) larger than that of the unfilled PEI polymer, in the case of that the volume fraction of BN nanoparticles is exceptionally small, only $c_{\mathtt{p}} = 0.0062$. This enhancement cannot be explained solely by the perfect bonding or the presence of interphases, between the polymer and the nanoparticles. On the contrary, the close agreement possible between the theoretical results and the experimental data shown in Figs. 6.3(e) and (f) suggests that the presence of active space charges might indeed be the mechanism responsible for the observed enhanced dielectric response.

6.4 The experiments of Nelson and Fothergill (2004) on epoxy filled with TiO_2 nanoparticles

The next set of results that we consider are those presented in Fig. 6.4 due to Nelson and Fothergill (2004) for the dielectric response at a temperature of 393 K of a bisphenol-A epoxy isotropically filled with TiO_2 nanoparticles, with roughly spherical shape, 12 nm in average radius, and volume fraction $c_{\mathtt{p}} = 0.026$, under a uniform alternating electric field with frequencies ranging from 10^{-2} Hz to 1 MHz. Akin to the preceding figures, Figs. 6.4(a) and (b) display the comparsions between the experimental data (solid lines) and the theroretical

results in the absence of interphases and space charges, while Figs. 6.4(c) and (d) compare the experimental data with the theoretical results in the presence of interphases between the TiO_2 nanoparticles and the epoxy resin, and Figs. 6.4(e) and (f) show the comparisons between the experimental data and the theoretical results when space charges are accounted for. For direct comparison, all the plots in Fig. 6.4 include the corresponding response (dashed lines) of the unfilled epoxy resin, as reported by Nelson and Fothergill (2004). Note that, in contrast to the foregoing nanoparticulate composites wherein the addition of nanoparticles led to exceptionally large enhancements, the addition of TiO_2 nanoparticles here leads to a substantial *diminishment* of the dielectric response, in spite of the fact that TiO_2 features a larger (real part of the) permittivity than epoxy for most of the frequencies considered ($f > 10^{-1}$ Hz, at least).

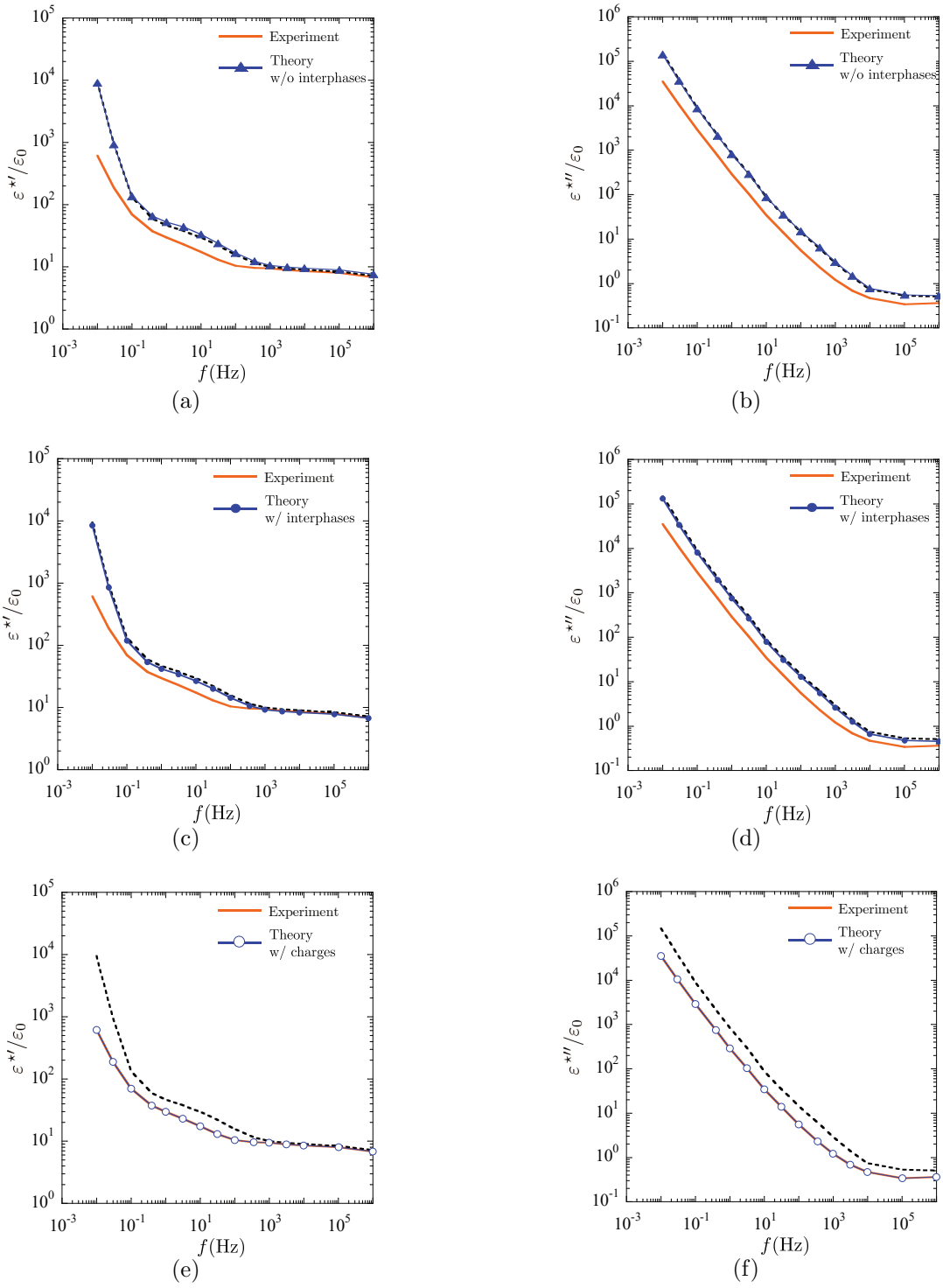

Figure 6.4: Comparisons between the experimental results (solid lines) of Nelson and Fothergill (2004) for an epoxy resin filled with TiO_2 nanoparticles and the proposed theoretical results: (a)-(b) without interphases (triangles), (c)-(d) with interphases (solid circles), and (e)-(f) with space charges (empty circles). The comparisons are shown for the real and complex parts of the effective complex permittivity $\widetilde{\varepsilon}^{\star}(\omega) = \varepsilon^{\star\prime}(\omega) - i\varepsilon^{\star\prime\prime}(\omega)$, normalized by the permittivity of vacuum ε_0, as functions of the frequency $f = \omega/2\pi$ of the applied electric field. All the plots include the corresponding experimentally measured response (dashed lines) of the unfilled epoxy resin.

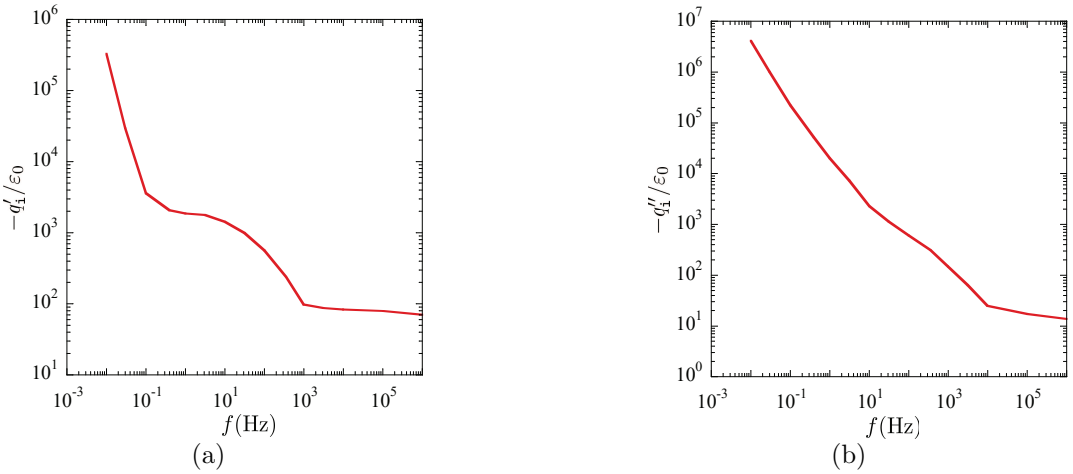

Figure 6.5: The complex space charge function $q_{\mathtt{i}}(\omega)$ utilized in the theoretical results presented in Fig. 6.4(e) and (f). Parts (a) and (b) show, respectively, the negative of the real and imaginary parts of the function $q_{\mathtt{i}}(\omega) = q'_{\mathtt{i}}(\omega) - iq''_{\mathtt{i}}(\omega)$, normalized by the permittivity of vacuum ε_0, as functions of the frequency $f = \omega/2\pi$ of the applied electric field.

Much like in the three preceding figures, all the theoretical results presented in Fig. 6.4 correspond to the formula (5.7) with $c_{\mathtt{p}} = 0.026$ where the complex permittivity for the epoxy $\widetilde{\varepsilon}_{\mathtt{m}}(\omega)$ takes the experimental values reported by Nelson and Fothergill (2004). These authors did not report the dielectric response for the TiO_2 nanoparticles that they used in their specimens. Accordingly, for definiteness, the complex permittivity $\widetilde{\varepsilon}_{\mathtt{p}}(\omega)$ of these in the formula (5.7) is characterized with the Havriliak-Negami model $(5.8)_2$ and the material parameters $\varepsilon_{\mathtt{p}_0} = 140\varepsilon_0$, $\varepsilon_{\mathtt{p}_\infty} = 104\varepsilon_0$, $\tau_{\mathtt{p}} = 2.560 \times 10^{-3}$ s, $\alpha_{\mathtt{p}} = 0.5788$, and $\beta_{\mathtt{p}} = 1.0228$, which were obtained by fitting the experimental data of Anithakumari et al. (2017) for a high purity TiO_2 in the frequency range 100 Hz to 1 MHz. The results in Fig. 6.4(a) and (b) correspond to the further prescription $c_{\mathtt{i}} = 0$, $q_i(\omega) = 0$, those in Figs. 6.4(c) and (d) to $c_{\mathtt{i}} = 0.050$, $q_i(\omega) = 0$, and $\widetilde{\varepsilon}_{\mathtt{i}}(\omega) = \varepsilon_0$, while those in Figs. 6.4(e) and (f) correspond to $c_{\mathtt{i}} = 0.050$, $\widetilde{\varepsilon}_{\mathtt{i}}(\omega) = \widetilde{\varepsilon}_{\mathtt{m}}(\omega)$, and a complex space charge function $q_{\mathtt{i}}(\omega) = q'_{\mathtt{i}}(\omega) - iq''_{\mathtt{i}}(\omega)$ with the real $q'_{\mathtt{i}}(\omega)$ and imaginary $q''_{\mathtt{i}}(\omega)$ parts plotted in Fig. 6.5. With respect to these prescriptions, we note that the choice of $c_{\mathtt{i}} = 0.050$ for the volume fraction of interphases implies an average interphase thickness of 5 nm. Again, since the average radius of the TiO_2 nanoparticles is 12 nm, such an average thickness is relatively large but realistic. Moreover, the choice $\widetilde{\varepsilon}_{\mathtt{i}}(\omega) = \varepsilon_0$ for the complex permittivity of the interphases is the one

that maximizes the reduction in the dielectric response of the composite. Lastly, we note that a complex space charge function $q_{\mathtt{i}}(\omega)$ characterized by the Havriliak-Negami relation (5.10) is not functionally rich enough to render good agreement with the experimental data. By construction, the choice of function $q_{\mathtt{i}}(\omega)$ plotted in Fig. 6.5, which was obtained by directly fitting the experimental data for $\varepsilon^{\star\prime}(\omega)$ and $\varepsilon^{\star\prime\prime}(\omega)$, does render good agreement.

From the comparisons presented in Figs. 6.4(a) and (b), it is clear that perfect bonding between the TiO_2 nanoparticles and the epoxy resin cannot possibly explain the reduction in the dielectric response featured by this composite. As shown by Figs. 6.4(c) and (d), the presence of low-permittivity interphases might help to explain some of the reduction, but not the bulk of it. On the other hand, the comparisons presented in Figs. 6.4(e) and (f) indicate that the reduction in the dielectric response of this nanoparticulate composite might be explained in full by the presence of space charges.

6.5 The experiments of Fothergill et al. (2004) on epoxy filled with ZnO nanoparticles

The last experiments from Fothergill et al. (2004) are at a temperature of 393 K of a bisphenol-A epoxy isotropically filled with ZnO nanoparticles, with roughly spherical shape, 12 nm in average radius, and volume fraction $c_{\mathtt{p}} = 0.02$, under a uniform alternating electric field with frequencies ranging from 10^{-3} Hz to 1 MHz. Again, parts (a)-(b) and (c)-(d) in Fig. 6.6 compare the experimental data (solid lines) with the theoretical results in the absence of space charges when interphases between the ZnO nanoparticles and the epoxy resin are absent and present, respectively, while parts (e)-(f) display the comparisons between the experimental data and the theoretical results for the case when space charges are accounted for. For direct comparison, all the plots in Fig. 6.6 include the corresponding response (dashed lines) of the unfilled epoxy resin, as reported by Fothergill et al. (2004). Like the Section 6.4, the addition of ZnO nanoparticles here leads to a substantial *diminishment* of the dielectric response, in spite of the fact that ZnO features a larger (real part of the) permittivity than epoxy for most of the frequencies considered ($f > 10^{-2}$ Hz, at least).

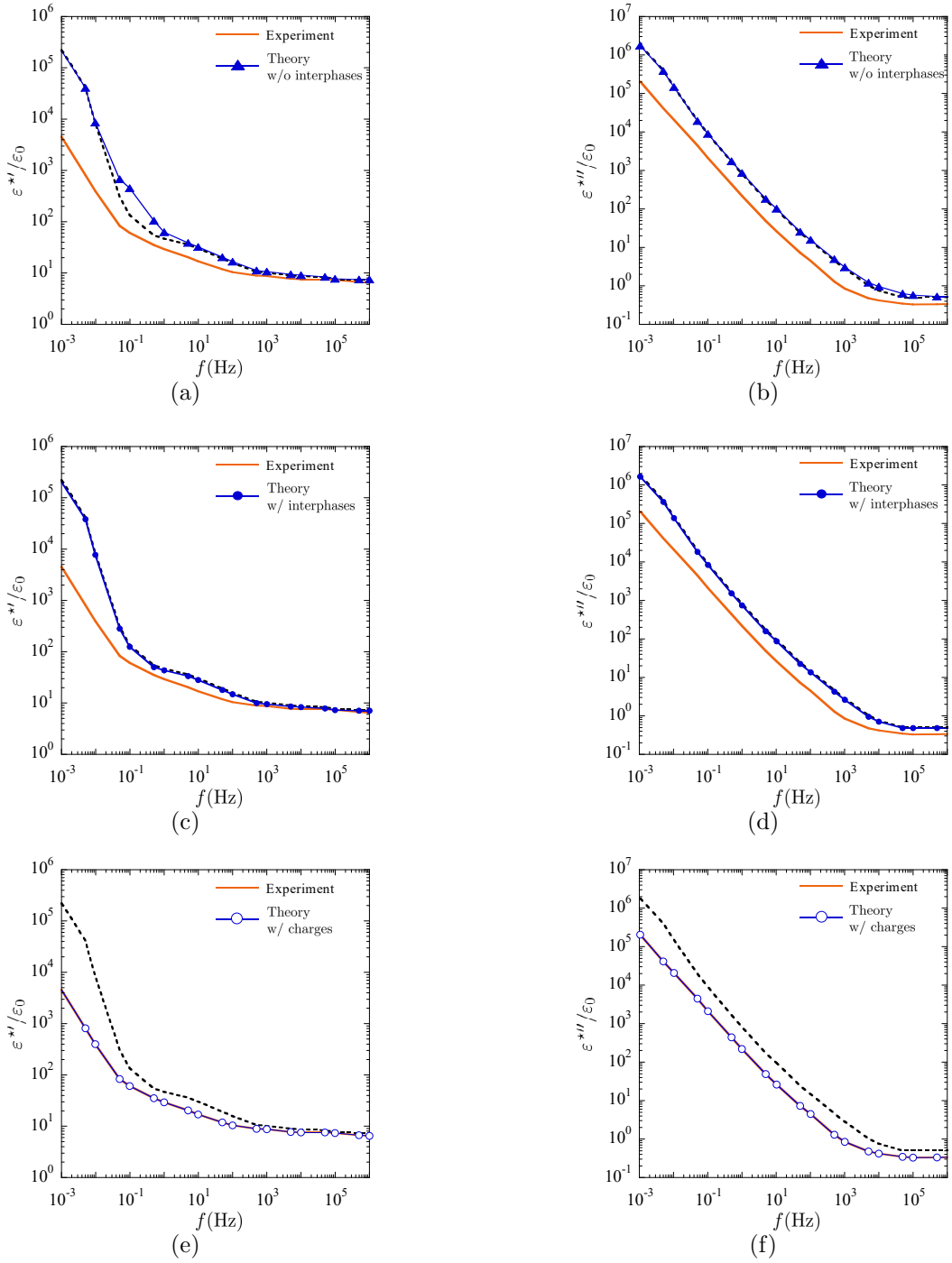

Figure 6.6: Comparisons between the experimental results (solid lines) of Fothergill et al. (2004) for an epoxy resin filled with ZnO nanoparticles and the proposed theoretical results: (a)-(b) without interphases (triangles), (c)-(d) with interphases (solid circles), and (e)-(f) with space charges (empty circles). The comparisons are shown for the real and complex parts of the effective complex permittivity $\widetilde{\varepsilon}^{\star}(\omega) = \varepsilon^{\star\prime}(\omega) - i\varepsilon^{\star\prime\prime}(\omega)$, normalized by the permittivity of vacuum ε_0, as functions of the frequency $f = \omega/2\pi$ of the applied electric field. All the plots include the corresponding experimentally measured response (dashed lines) of the unfilled epoxy resin.

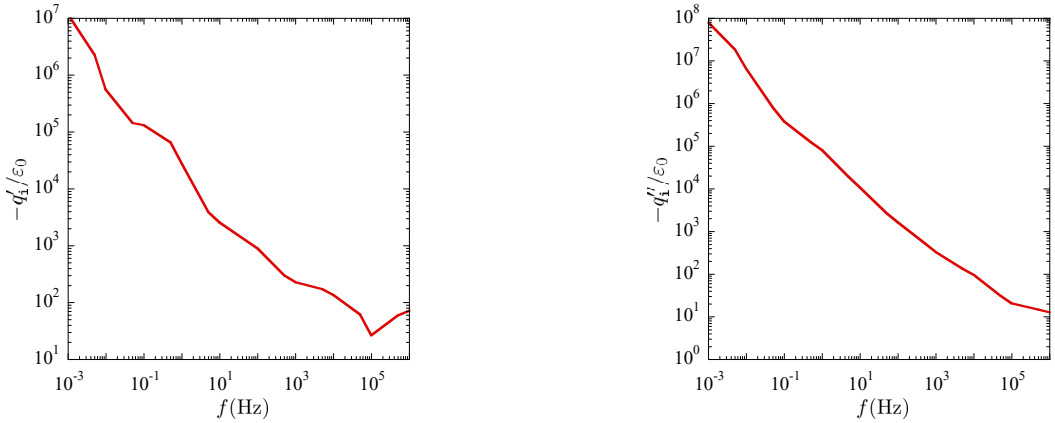

Figure 6.7: The complex space charge function $q_{\mathtt{i}}(\omega)$ utilized in the theoretical results presented in Fig. 6.6(e) and (f). Parts (a) and (b) show, respectively, the negative of the real and imaginary parts of the function $q_{\mathtt{i}}(\omega) = q_{\mathtt{i}}'(\omega) - iq_{\mathtt{i}}''(\omega)$, normalized by the permittivity of vacuum ε_0, as functions of the frequency $f = \omega/2\pi$ of the applied electric field.

Akin to the preceding figures, all the theoretical results presented in Figs. 6.6 correspond to the formula (5.7) with $c_{\mathtt{p}} = 0.02$ where the complex permittivity for the epoxy $\widetilde{\varepsilon}_{\mathtt{m}}(\omega)$ takes the experimental values reported by Fothergill et al. (2004), which however, did not report the dielectric response for the ZnO particles. Accordingly, for definiteness, the complex permittivity $\widetilde{\varepsilon}_{\mathtt{p}}(\omega)$ of these in the formula (5.7) is characterized with the Havriliak-Negami model $(5.8)_2$ and the material parameters $\varepsilon_{\mathtt{p}_0} = 9000\varepsilon_0$, $\varepsilon_{\mathtt{p}_\infty} = 10\varepsilon_0$, $\tau_{\mathtt{p}} = 7.810 \times 10^{-3}$ s, $\alpha_{\mathtt{p}} = 1.0$, and $\beta_{\mathtt{p}} = 0.8706$, which were obtained by fitting the experimental data of Varshney et al. (2015) for a high purity ZnO in the frequency range 50 Hz to 1 MHz. The results in Figs. 6.6(a) and (b) correspond to the further prescription $c_{\mathtt{i}} = 0$, $q_i(\omega) = 0$, those in Figs. 6.6(c) and (d) to $c_{\mathtt{i}} = 0.036$, $q_i(\omega) = 0$, and $\widetilde{\varepsilon}_{\mathtt{i}}(\omega) = \varepsilon_0$, while those in Figs. 6.6(e) and (f) correspond to $c_{\mathtt{i}} = 0.036$, $\widetilde{\varepsilon}_{\mathtt{i}}(\omega) = \widetilde{\varepsilon}_{\mathtt{m}}(\omega)$, and a complex space charge function $q_{\mathtt{i}}(\omega) = q_{\mathtt{i}}'(\omega) - iq_{\mathtt{i}}''(\omega)$ with the real $q_{\mathtt{i}}'(\omega)$ and imaginary $q_{\mathtt{i}}''(\omega)$ parts plotted in Fig. 6.7. Regarding of these prescriptions, we mark again the choice of $c_{\mathtt{i}} = 0.036$ for the volume fraction of interphases comes from the average interphase thickness of 5 nm. Again, such an average thickness is relatively large but realistic, considering that the avarage radius of the ZnO nanoparticles is 12 nm. Specifically, the choice of function $q_{\mathtt{i}}(\omega)$ plotted in Fig. 6.7 was obtained by directly fitting the experimental data for $\varepsilon^{\star\prime}(\omega)$ and $\varepsilon^{\star\prime\prime}(\omega)$ to render a good agreement.

From all the comparisons presented in Figs.6.6 (a)-(d), the reduction in the dielectric response of this composite cannot be explained simply by the perfect bonding between the ZnO nanoparticles and the epoxy resin, and it is not sufficient to explain the whole reduction with the aid of interphases between the polymer and nanoparticles—whereas, the comparisons displayed in Figs. 6.6(e) and (f) indicate that the presence of space charges might be accounted for the observed reduced dielectric response of this composite.

CHAPTER 7

CONCLUDING REMARKS

At the close of this thesis, it is important to remark that the corresponding theoretical results for a simple cubic distribution of monodisperse spherical particles outlined in Section 5.1 are virtually indistinguishable from those presented in Chpater 6 for the random isotropic distribution of polydisperse spherical particles outlined in Section 5.2; the former were generated numerically via the finite-element formulation presented in the Appendix of Spinelli et al (2015). This agreement suggests that the specifics of the distribution in space and the dispersion in size of the filler nanoparticles in isotropic polymer nanoparticulate composites with small volume fractions of nanoparticles are of little consequence for their macroscopic dielectric response. A number of calculations have been presented for random distributions of non-spherical particles akin to those presented in Section 6 of Lefèvre and Lopez-Pamies (2017b) and the conclusions are the same, namely, the specifics of the shape of the nanoparticles have little impact on the macroscopic response provided that the content of nanoparticles is sufficiently away from percolation. This insensitivity to the spatial distribution, the size, and the shape of the nanoparticles further strengthens the conjecture made here that the presence of active space charges is the mechanism behind the extreme dielectric response of emerging polymer nanoparticulate composites. By the same token, more generally, it also points to the manipulation of space charges at small length scales as a promising path towards the design of materials with exceptional macroscopic properties.

REFERENCES

[1] Anithakumari, P., Mandal, B.P., Nigam, S., Majumder, C., Mohapatra, M., Tyagi, A.K., 2017. Experimental and theoretical investigation of the high dielectric permittivity of tantalum doped titania. *New Journal of Chemistry* 41, 13067–13075.

[2] Bauer, S., Gerhard-Multhaupt, R., Sessler, G.M., 2004. Ferroelectrets: Soft electroactive foams for transducers. *Physics Today* 57, 37–43.

[3] Bensoussan, A., Lions, J.L., Papanicolau, G., 2011. *Asymptotic Analysis for Periodic Structures*. AMS Chelsea Pubishing, Providence.

[4] Brochu, P., Pei, Q., 2013. Advances in dielectric elastomers for actuators and artificial muscles*Macromolecular rapid communications* 31(1), 10-36.

[5] Böttcher, C.J.F., Bordewijk, P., 1978. *Theory of Electric Polarization, Vol. II. Dielectrics in Time-Dependent Fields*. Elsevier Amsterdam, Oxford.

[6] Bar-Cohen, Y., 2004. *Electroactive polymer (EAP) actuators as artificial muscles: reality, potential, and challenges, Vol. 136*. Bellingham, WA: SPIE press.

[7] Chew, W.C., Sen, P.N., 1982. Dielectric enhancement due to electrochemical double layer: Thin double layer approximation. *J. Chem. Phys.* 77, 4683–4693.

[8] Cole, K.S., Cole, R.H., 1941. Dispersion and absorption in dielectrics I. Alternating current characteristics. *J. Phys. Chem.* 9, 341–351.

[9] Carpi, F., Smela, E., 2009. *Biomedical applications of electroactive polymer actuators*. John Wiley & Sons.

[10] Davidson, D.W., Cole, R.H., 1951. Dielectric relaxation in glycerol, propylene glycol, and n-propanol. *J. Phys. Chem.* 19, 1484–1490.

[11] Debye, P., 1929. *Polar Molecules*. Dover Publications, New York.

[12] Friedrich, K., Schönhals, A. (Editors), 2003. *Broadband Dielectric Spectroscopy*. Springer-Verlag, Berlin.

[13] Fothergill,J., Nelson, J., Fu, M., 2004. Dielectric properties of epoxy nanocomposites containing TiO_2, Al_2O_3 and ZnO fillers. *In The 17th Annual Meeting of the IEEE Lasers and Electro-Optics Society*, 406-409.

[14] Garrappa, R., Mainardi, F., Guido, M., 2016. Models of dielectric relaxation based on completely monotone functions. *Fractional Calculus and Applied Analysis* 19, 1105–1160.

[15] Gross, B., 1953. *Mathematical Structure of the Theories of Viscoelasticity*. Hermann, Paris.

[16] Hashin, Z., 1962. The elastic moduli of heterogeneous materials. *Journal of Applied Mechanics* 29, 143–150.

[17] Hashin, Z., 1983. Analysis of composite materials — A survey. *Journal of Applied Mechanics* 50, 481–505.

[18] Havriliak, S., Negami, S., 1966. A complex plane analysis of α-dispersions in some polymer systems. *J. Polym. Sci. C* 14, 99–117.

[19] Huang, C., Zhang, Q.M., Li, J.Y., Rabeony, M., 2005. Colossal dielectric and electromechanical responses in self-assembled polymeric nanocomposites. *Applied Physics Letters* 87, 182901.

[20] Kestelman, V.N., Pinchuk, L.S., Goldade, V.A., 2000. *Electrets In Engineering: Fundamentals and Applications*. Springer, New York.

[21] Lewis, T.J., 2004. Interfaces are the dominant feature of dielectrics at the nanometric level. *IEEE Transactions on Dielectrics and Electrical Insulation* 11, 739–753.

[22] Lopez-Pamies, O., Goudarzi, T., Meddeb, A.B., Ounaies, Z., 2014. Extreme enhancement and reduction of the dielectric response of polymer nanoparticulate composites via interphasial charges. *Applied Physics Letters* 104, 242904.

[23] Lefèvre, V., Lopez-Pamies, O., 2017a. Homogenization of elastic dielectric composites with rapidly oscillating passive and active source terms. *SIAM Journal on Applied Mathematics* 77, 1962–1988.

[24] Lefèvre, V., Lopez-Pamies, O., 2017b. Nonlinear electroelastic deformations of dielectric elastomer composites: I — Ideal elastic dielectrics. *Journal of the Mechanics and Physics of Solids* 99, 409–437.

[25] Lefèvre, V., Lopez-Pamies, O., 2017c. Nonlinear electroelastic deformations of dielectric elastomer composites: II — Non-Gaussian elastic dielectrics. *Journal of the Mechanics and Physics of Solids* 99, 438–470.

[26] Meddeb, A.B., Tighe, T., Ounaies, Z., Lopez-Pamies, O., 2019. Extreme enhancement of the nonlinear elastic response of elastomer nanoparticulate composites via interphases. *Composites Part B* 156, 166–173.

[27] Milton, G.W., 2002. *The Theory of Composites*. Cambridge University Press.

[28] Nelson, J.K. (Editor), 2010. *Dielectric Polymer Nanocomposites*. Springer, New York.

[29] Nelson, J.K., Fothergill, J.C., 2004. Internal charge behaviour of nanocomposites. *Nanotechnology* 15, 586–595.

[30] Owen, G.E., 2003. *Introduction to Electromagnetic Theory*. Dover, Mineola.

[31] Qu, M., Deng, F., Kalkhoran, S.M., Gouldstone, A., Robisson, A., Van Vliet, K.J., 2011. Nanoscale visualization and multiscale mechanical implications of bound rubber interphases in rubber–carbon black nanocomposites. *Soft Matter* 7, 1066–77.

[32] Roy, M., Nelson, J.K., MacCrone, R.K., Schadler, L.S., Reed, C.W., Keefe, R., Zenger, W., 2005. Polymer nanocomposites dielectrics — The role of the interface. *IEEE Transactions on Dielectrics and Electrical Insulation* 12, 629–643.

[33] Sanchez-Palencia, E., 1980. *Nonhomogeneous Media and Vibration Theory*, Lect. Notes Phys. 127, Springer, New York.

[34] Sanchez-Hubert, J., Sanchez-Palencia, E., 1978. Sur certains problèmes physiques d'homogénéisation donnant lieu à des phénomènes de relaxation. *Compt. Rend. Acad. Sci. Paris A.* 286, 903–906.

[35] Schwan, H.P., Schwarz, G., Maczuk, J., Pauly, H., 1962. On the low-frequency dielectric dispersion of colloidal particles in electrolyte solution. *J. Phys. Chem.* 66, 2626–2635.

[36] Sillars, R.W., 1936. The properties of a dielectric containing semiconducting particles of various shapes. *Journal of the Institute of Electrical Engineers* 12, 378–394.

[37] Spinelli, S.A., Lefèvre, V., Lopez-Pamies, O., 2015. Dielectric elastomer composites: A general closed-form solution in the small-deformation limit. *Journal of the Mechanics and Physics of Solids* 83, 263–284.

[38] Tartar, L., 2009. *The General Theory of Homogenization*. Springer-Verlag Berlin Heidelberg.

[39] Thakur, Y., Zhang, T., Iacob, C., Yang, T., Bernholc, J., Chen, L.Q., Runt, J., Zhang, Q.M., 2017. Enhancement of the dielectric response in polymer nanocomposites with low dielectric constant fillers. *Nanoscale* 9, 10992–10997.

[40] Vila, R., Gonzalez, M., Molla, J., Ibarra, A., 1998. Dielectric spectroscopy of alumina ceramics over a wide frequency range. *Journal of Nuclear Materials* 253, 141–148.

[41] Varshney, D., Verma, K., Dwivedi, S., 2015. Structural and dielectric studies of hexagonal ZnO nanoparticles. *Optik* 126(23), 4232-4236.

[42] Wagner, K.W., 1914. Erkläirung der dielektrischen nachwirkungsvorgäinge auf firund Maxwellscher vorstellungen. Archiv für Elektrotechnik 2, 371–387.

[43] Wang, J.-W., Shen, Q.-D., Bao, H.-M., Yang, C.-Z., Zhang, Q.M., 2005. Microstructure and dielectric properties of P(VDF-TrFE-CFE) with partially grafted copper phthalocyanine oligomer. *Macromolecules* 38, 2247–2252.

[44] Zhang, T., Thakur, Y., Zhang, Q.M., 2017. Doped dielectric polymers with low dielectric constant nanofillers. *2017 IEEE Conference on Electrical Insulation and Dielectric Phenomenon (CEIDP)* 437-440.